

NEW METHOD FOR CYRSTAL ORIENTATION ANALYSIS OF MINERAL SAMPLES
AND APPLICATION TO THE MICROSTRUTURE AND FORMATION OF OOIDS

Matthew J. Frazier

Advisor: Prof. Pupa Gilbert

Department of Physics

University of Wisconsin- Madison

In partial fulfillment of the degree of:
Bachelor of Science in Physics with Honors

TABLE OF CONTENTS

- I. Introduction 3
- II. Acknowledgements 3
- III. Multi-wavelength LC-PolScope Method for High Retardance Samples 4
 - A. Design and Principles of Operation of the LC-PolScope. 5
 - B. Multi-wavelength Augmented Procedures for High Retardance Samples. 9
 - C. Example Aragonite Data Using MPS, and Comparison with Other Methods. 11
- IV. Crystal Orientation Analysis of Ooids at the Microscale 16
 - A. Background. 16
 - B. Results. 18
 - C. Discussion. 24
 - D. Conclusions. 26
- V. References. 26
- VI. Appendix I. 29
- VII. Appendix II. 33

INTRODUCTION

The primary motivation for this thesis was to analyze at the microscale the crystal orientations in ooids, that is, roughly spherical carbonate grains, which form in shallow tidal marine environments. However, due to the limitations and limited accessibility of methods to do so (namely Electron Backscatter Diffraction (EBSD) and Polarization Imaging Contrast (PIC) mapping) we chose another method, which is readily accessible, accurate, and provides a fast way to quantitatively map crystal orientations at the microscale: polarized light microscopy using a new approach termed Multi-wavelength PolScope (MPS), which opens up a new and promising area of research. Various methods have been developed fairly recently to map crystal orientation or other useful information using polarized light microscopy, with various applications in mind (Heilbronner & Pauli, 1993; Glazer, Lewis, & Kaminsky, 1996; Oldenbourg & Mei 1995). The Liquid Crystal (LC)-PolScope is one of the most widely used, and has in fact been used to image carbonate samples before (Oldenbourg, 2008; Volkmer et. al., 2005; Eder et. al., 2010). However, the only studies that successfully imaged carbonates using the LC-PolScope focused on very thin samples, and it became quickly apparent that some modification was needed. This Multi-wavelength PolScope (MPS) modification, developed by us for the first time, is described in the first section of this thesis.

The second section is devoted to the crystal orientation analysis of ooids. Although ooids have been extensively studied since the late 19th century, relatively little is known about their formation mechanism. Since ooids are found throughout the geologic record, determining the mechanism of their formation could be important for determining the environments present at the time of the formation of ancient ooids. Though there have been many studies of the microstructure of ooids using Scanning Electron Microscopy (SEM), only very limited analysis of the crystal orientation of ooids has been done to my knowledge. It should be noted that most authors also use the term ooid to describe spherulitic structures forming in shallow marine environments, but in this study only “classical” tangential ooids that formed in the present day are considered.

ACKNOWLEDGEMENTS

As well as my mentor Pupa Gilbert, I would like to thank Chang-Yu Sun for much guidance over the last two years, as well as Cayla Stifler and Jay Zhang. Matthew Marcus of the Advanced Light Source (ALS) also provided invaluable discussion and suggestions regarding the development of data processing of Multi-wavelength LC-PolScope data. LC-PolScope experiments were done at the Laboratory for Optical and Computational Imaging (LOCI) at UW-Madison in collaboration with Adib Keikhosravi and

Kevin Eliceiri. Ooid samples were provided by our collaborator Prof. Kristin Bergmann of MIT, who also welcomed us to her lab for several days in June 2017. Finally, I was supported by the Hilldale Scholarship for Undergraduate Research and Pupa Gilbert's grants DOE DE-FG02-07ER15899 and NSF DMR-1603192 for travels to MIT and to the ALS in Berkeley in April 2018.

MULTI-WAVELENGTH LC-POLSCOPE METHOD FOR HIGH-RETARDANCE SAMPLES

The LC-PolScope, originally described by Oldenbourg & Mei (1995), is a method for imaging retardance and in-plane slow axis orientation of birefringent media in thin section. To provide a brief glossary of terminology, these words have the following meanings:

Birefringent materials: materials in which the index of refraction varies depending on the linear polarization angle of the incident light.

Uniaxial crystals: crystals that exhibit a slow axis (with higher index of refraction) and a fast axis (with lower index of refraction) which are oriented perpendicular to each other.

Birefringence: is the difference between the index of refraction along the slow axis and the index of refraction along the fast axis.

Retardance: is defined as the birefringence times the path length of the light inside the medium, or the path difference between light travelling along the fast and slow axes respectively. In the case of transmitted light microscopy, the birefringence is thus thickness of the sample times birefringence.

Liquid Crystal (LC)-PolScope: Technique for imaging slow axis orientation and retardance in thin sections with low retardance using a transmitted light microscope with elliptical polarizer.

Multi-wavelength PolScope (MPS): Augmented LC-PolScope technique for measuring slow-axis orientation and retardance in high-retardance samples by taking LC-PolScope images at multiple wavelengths.

The LC-PolScope was designed with biological specimens in mind and has been used with great success in imaging collagen (Frano et. al., 2009; Rosin et. al., 2016; Keikhosravi et. al., 2018). However, a large class of birefringent media, birefringent crystals, has not been successfully imaged, except in some special cases, with the LC-PolScope. The principal limitation when imaging crystals with the LC-PolScope is that only retardances of up to one half the working wavelength can be directly measured using the PolScope, and orientation measurements of crystals outside this retardance range may not be accurate. Biological media often only exhibit a small amount of birefringence, or exhibit form birefringence, caused by internal stress in a small structure and this is a very small effect when compared to the intrinsic birefringence of most birefringent media (Bragg & Pipper, 1953). Meanwhile birefringent

crystals can have a much larger birefringence. For example, the birefringence of collagen varies, but is on the order of 10^{-3} (Maitland & Walsh, 1997; Vidal, 1970), while aragonite and calcite, the stable polymorphs of calcium carbonate (CaCO_3), have birefringences of 0.156 and 0.174 respectively (Bragg, 1924). In addition, while techniques such as ultramicrotomy allow biological samples to be accurately thinned to thicknesses on the order of only a few tens of nanometers, the hardness of minerals prevents them from being sectioned with a microtome. Traditional grinding methods cannot be used to reliably thin samples to less than $10\ \mu\text{m}$, making the typical minimum retardance of a carbonate thin section on the order of $1\ \mu\text{m}$, far higher than the $\frac{1}{2}$ wavelength restriction imposed by the PolScope for any visible wavelength. Thus, while the LC-PolScope has been used successfully in imaging carbonates grown in thin films ($\sim 1\ \mu\text{m}$ thick) (Oldenbourg, 2008; Volkmer et. al., 2005), it has been impossible to use this technique to accurately image most three-dimensional carbonate samples, and other high-birefringence mineral samples.

In the sections below, I will briefly describe the data acquisition and processing procedure used to obtain LC-PolScope data, with emphasis on the maximum retardance limitation. Next, I will describe the newly developed, MPS augmented data acquisition and processing procedure using the LC-PolScope which allows accurate retardance and slow-axis orientation imaging of carbonate crystals, or samples with high retardance in general. Results using this new procedure are then presented and compared to crystal orientation measurements of similar samples using well-established methods.

A. DESIGN AND PRINCIPLES OF OPERATION OF THE LIQUID CRYSTAL (LC)-POLSCOPE

The physical setup of the LC-PolScope is described in detail by Oldenbourg (2003) and the data processing algorithms are described in detail by Shribak & Oldenbourg (2003). The description below is taken from Shribak & Oldenbourg (2003), and complete details can be found therein. The description below is shortened.

LC-PolScope design is based on the basic setup of the traditional petrographic microscope. The microscope works in transmission, with a polarizer placed in the light path before the sample, and another polarizer termed analyzer in the light path after the sample, before the eyepiece or camera. In a traditional petrographic microscope, the polarizer and analyzer are both linear polarizers, placed at 90° from one another, so that only birefringent samples, which alter the polarization state as light passes through the sample, appear bright, on a dark background of optically inactive sample parts. Instead of a linear polarizer before the sample, the LC-PolScope uses a variable elliptical polarizer, made up of four components: a linear polarizer, a bandpass filter (centered around the wavelength λ), and two variable-retardance liquid crystals with their slow-axes at an angle of 45° with respect to each other. By applying

a voltage the birefringence of the two liquid crystals changes, and thus their retardance changes. The linear polarizer is set at an orientation of 45° with respect to the first liquid crystal. The thickness of each liquid crystal is such that, with no voltage applied, one liquid crystal is a $\lambda/4$ waveplate, and the other is a $\lambda/2$ waveplate. The combination of these four components produces right circularly polarized light when no voltage is applied. In place of a linear analyzer, the LC-PolScope uses a left circular analyzer ($\lambda/4$ waveplate). Thus when there is no voltage applied to the elliptical polarizer before the sample, only birefringent media will be imaged, much the same as in the traditional petrographic microscope. A schematic of the light path is shown in Figure 1. Switching the order of the elliptical polarizer and the left-circular analyzer produces the same results, as shown in Figure 1(b).

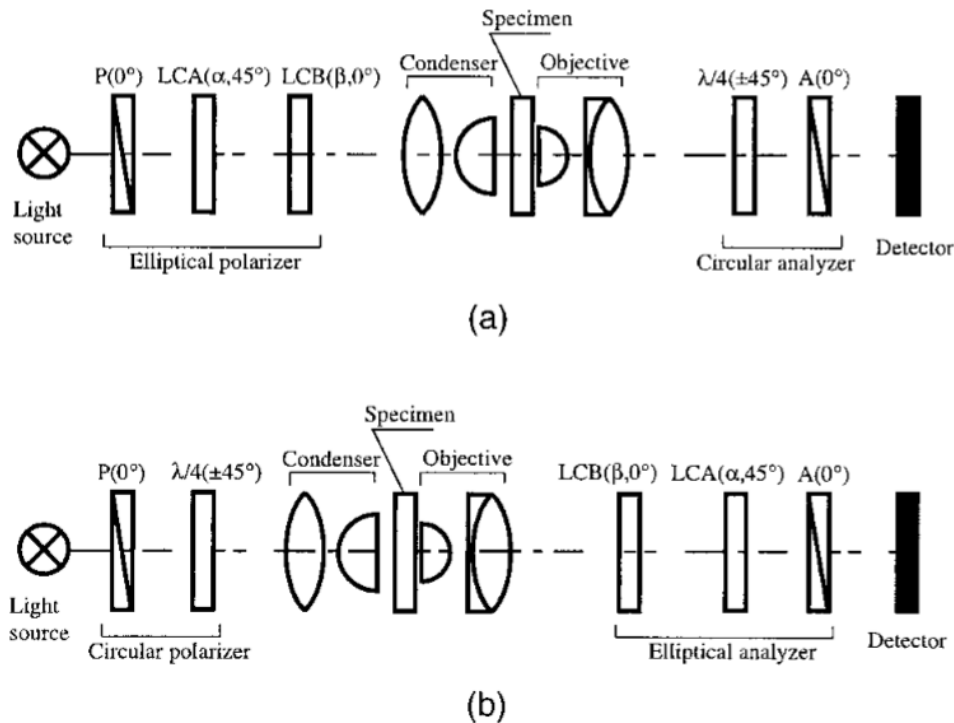


Figure 1: Schematic of light path in the LC-PolScope, taken from Shribak & Oldenbourg 2003. (a) is the setup described in the text, while (b) is a setup in which the order of the elliptical polarizer and circular polarizer is switched, producing equivalent results. P and A are linear polarizers (Polarizer and Analyzer), and the first liquid crystal is labeled LCA, the second LCB, with retardances of α and β respectively.

The LC-PolScope takes five images of a sample, each with a well-defined polarization state. The first image is acquired with the sample illuminated by right circularly polarized light, and the other four with elliptically polarized light, with major axes oriented at 0° , 45° , 90° , and 135° with respect to the linear polarizer in the elliptical polarizer before the sample. These five elliptically polarized states are produced

by respectively adding and subtracting a set retardance from (applying a voltage to) each liquid crystal separately. This added or subtracted retardance is expressed in fraction of wavelength, χ . For small values of χ , the ellipticity of the polarized light, b/a , where b is the semimajor axis, and a is the semiminor axis, can be approximated as

(1)

$$\frac{b}{a} = 1 - \pi\chi$$

Thus, elliptical states with major axes at 0° and 90° are made by respectively subtracting and adding a retardance $\lambda \cdot \chi$ from the first compensator. Similarly, elliptical states with major axis oriented at 45° and 135° are made by respectively subtracting and adding a retardance χ from the second compensator. Denoting the total retardance of the first liquid crystal compensator as α and the second as β , the five polarization states are defined by:

(2)

$$\begin{aligned} \epsilon_1: \quad \alpha_1 &= \lambda/4 & \beta_1 &= \lambda/2 \\ \epsilon_2: \quad \alpha_2 &= \lambda/4 - \chi \cdot \lambda & \beta_2 &= \lambda/2 \\ \epsilon_3: \quad \alpha_3 &= \lambda/4 & \beta_3 &= \lambda/2 - \chi \cdot \lambda \\ \epsilon_4: \quad \alpha_4 &= \lambda/4 + \chi \cdot \lambda & \beta_4 &= \lambda/2 \\ \epsilon_5: \quad \alpha_5 &= \lambda/4 & \beta_5 &= \lambda/2 + \chi \cdot \lambda \end{aligned}$$

Combining the effects of the sample retardance with the elliptical polarizer and left circular analyzer, one can derive an expression for transmitted intensity for each pixel in an image

(3)

$$\begin{aligned} I(a, b, x, y) &= \frac{1}{2} \tau(x, y) I_{\max}(x, y) [1 + \sin(a) \cos(b) \cos(2\pi \cdot \Delta(x, y)/\lambda) - \\ &\quad \sin(a) \sin(b) \cos(2\phi(x, y)) \sin(2\pi \cdot \Delta(x, y)/\lambda) + \\ &\quad \cos(a) \sin(2\phi(x, y)) \sin(2\pi \cdot \Delta(x, y)/\lambda)] + I_{\min}(x, y) \end{aligned}$$

Here $a = 2\pi\alpha/\lambda$ and $b = 2\pi\beta/\lambda$, $\phi(x, y)$ is the in-plane slow axis orientation of the sample at a given pixel position (x, y) , the working wavelength λ , and $\Delta(x, y)$ the retardance of the sample at the same pixel position (x, y) . $I_{\min}(x, y)$ represents any depolarized background, while $\tau(x, y)$ is the isotropic sample transmittance, and $I_{\max}(x, y)$ is the illumination distribution. Substituting the five polarization states (2) into (3), gives expressions for the intensity of each state at each pixel ($I_{\epsilon_1}(x, y)$, $I_{\epsilon_2}(x, y)$, etc.) and combining these intensities as below results in three useful coefficients:

(4)

$$A = \frac{I_2 - I_3}{I_2 + I_3 - 2I_1} \tan\left(\frac{\chi}{2}\right) = \sin(2\phi) \tan(2\pi \cdot \Delta/\lambda)$$
$$B = \frac{I_4 - I_5}{I_4 + I_5 - 2I_1} \tan\left(\frac{\chi}{2}\right) = \cos(2\phi) \tan(2\pi \cdot \Delta/\lambda)$$
$$C = I_2 + I_3 - 2I_1 = \tau I_{\max}(1 - \cos(\chi)) \cos(2\pi \cdot \Delta/\lambda)$$

In turn, if we assume $0 \leq \Delta < \lambda/2 \Rightarrow \sin(2\pi\Delta/\lambda) \geq 0$, we can calculate

(5)

$$\Delta = \frac{\lambda}{2\pi} \left(\arctan([A^2 + B^2]^{1/2}) \right) \quad \text{if } C \geq 0$$
$$\Delta = \frac{\lambda}{2\pi} \left(\pi - \arctan([A^2 + B^2]^{1/2}) \right) \quad \text{if } C < 0$$

and

(6)

$$\phi = \frac{1}{2} \text{atan2}(A, B) \quad \text{if } C > 0$$
$$\phi = \frac{1}{2} \text{atan2}(-A, -B) \quad \text{if } C < 0$$

using the conventional atan2 function

(7)

$$\text{atan2}(y, x) = \arctan\left(\frac{y}{x}\right) \quad \text{if } x \geq 0$$
$$\text{atan2}(y, x) = \pi + \arctan\left(\frac{y}{x}\right) \quad \text{if } x < 0$$

These conventions are chosen assuming $\sin(2\pi\Delta/\lambda)$ is positive since there is otherwise no way of telling whether the sign of $\sin(2\pi\Delta/\lambda)$ is positive or negative .

It is clear from (7) that if $\Delta > \lambda/2$, Δ is not necessarily given correctly, since $[A^2 + B^2]^{1/2} = |\tan(2\pi\Delta/\lambda)|$. For example, if $C < 0 \Rightarrow \cos(2\pi\Delta/\lambda) < 0$ and $\sin(2\pi\Delta/\lambda) < 0$, then $2\pi\Delta/\lambda$ is in Quadrant III, so $\Delta = \frac{\lambda}{2\pi} (\pi + \arctan(2\pi\Delta/\lambda))$, not the value given in (5). In addition, even if atan2 could be used to calculate Δ , it would only give the correct output modulo 2π so if $\Delta > \lambda$, the retardance certainly cannot be calculated correctly. To solve this problem for high retardance samples such as carbonates we developed the MPS augmented method.

B. MULTI-WAVELENGTH POLSCOPE (MPS) AUGMENTED PROCEDURES FOR HIGH RETARDANCE SAMPLES

In the last section, I presented a concise derivation of the equations for slow-axis orientation and retardance as calculated by the LC-PolScope and highlighted the necessity that $\Delta \leq \lambda/2$. In this section, I will assume a high-retardance sample of retardance δ and a slow-axis orientation θ for the crystal being analyzed. It should be noted that in this formalism, while equations (5) and (6) still hold, the coefficients A, B, and C are now defined as:

(8)

$$\begin{aligned} A &= \frac{I_2 - I_3}{I_2 + I_3 - 2I_1} \tan\left(\frac{\chi}{2}\right) = \sin(2\theta)\tan(2\pi \cdot \delta/\lambda) \\ B &= \frac{I_4 - I_5}{I_4 + I_5 - 2I_1} \tan\left(\frac{\chi}{2}\right) = \cos(2\theta)\tan(2\pi \cdot \delta/\lambda) \\ C &= I_2 + I_3 - 2I_1 = \tau I_{\max}(1 - \cos(\chi))\cos(2\pi \cdot \delta/\lambda) \end{aligned}$$

From the equations 4-7 in the previous section, I will derive the lineshape for $\Delta(\delta, \lambda)$, the retardance measured by the conventional LC-PolScope, as a function of δ and λ , and $\theta(\phi, \delta, \lambda)$, where ϕ is the slow axis orientation measured by the conventional LC-PolScope. By taking data at multiple wavelengths, one may then perform a least-squares fit to $\Delta(\delta, \lambda)$ to find the value of δ , and then use this value to calculate $\theta(\phi, \delta, \lambda)$, obtaining accurate retardance and slow-axis orientation data for high-retardance samples.

We can see easily by the definition of A and B that equation (8) is true for all retardance values with one small modification:

(9)

$$\begin{aligned} \theta &= \frac{1}{2} \text{atan2}(A, B) \quad \text{if } \tan(2\pi\delta/\lambda) > 0 \\ \theta &= \frac{1}{2} \text{atan2}(-A, -B) \quad \text{if } \tan(2\pi\delta/\lambda) < 0 \end{aligned}$$

Assuming $\sin(2\pi\delta/\lambda) \geq 0$ as in the previous section makes this expression equivalent to equation (6), so if $0 < \delta(\text{mod}\lambda) < \frac{\lambda}{2}$, then $\theta = \phi$. Comparing equation (9) with equation (6) when $\sin(2\pi\delta/\lambda) < 0$ yields the equation:

(10)

$$\begin{aligned} \theta(\delta, \phi, \lambda) &= \phi \quad \text{if } 0 < \delta(\text{mod}\lambda) < \frac{\lambda}{2} \\ \theta(\delta, \phi, \lambda) &= \phi + \frac{\pi}{2} \quad \text{if } \frac{\lambda}{2} < \delta(\text{mod}\lambda) < \lambda \end{aligned}$$

Therefore, if δ can be accurately computed, then θ is easily computed as well. See Appendix I for a detailed derivation.

Similarly, we can compare the measured retardance Δ , with the actual retardance δ and derive an equation for $\Delta(\delta, \lambda)$, which is the measured retardance as a function of actual retardance and wavelength. As stated before, because of the periodic nature of trigonometric functions used, the calculation of Δ can be at best accurate modulo λ . Assuming $\sin(2\pi\delta/\lambda) \geq 0$ as in the first section, we get

$$\Delta = \delta(\text{mod } \lambda) \quad \text{if } 0 < \delta(\text{mod } \lambda) < \frac{\lambda}{2}$$

By analyzing equation (7) in the case that $\sin(2\pi\delta/\lambda) < 0$, can find an equation $\Delta(\delta, \lambda)$:

(11)

$$\Delta(\delta, \lambda) = (\delta \text{ (mod } \lambda)) \wedge (\lambda - \delta \text{ (mod } \lambda))$$

A quick analysis of (11) will confirm that $\Delta(\delta, \lambda) < \frac{\lambda}{2} \forall \lambda$. A detailed derivation can be found in Appendix I. Equation (11) is a relatively simple expression that suggests a way for finding δ by measuring Δ at various wavelengths to produce a set of pairs (λ_i, Δ_i) from which a least squares fit can be done to produce a value for δ . Once δ is calculated, θ can easily be calculated by equation (10).

Various wavelengths of approximately equal spacing across the visible range should be used for the best results. In the examples below, 7-8 different wavelengths were used and found sufficient. For each wavelength a different bandpass optical filter was placed in the elliptical polarizer, and the liquid-crystal retarders were calibrated to produce the five polarization states needed at that wavelength. Two factors complicate the fitting calculation of δ from fitting the data taken to $\Delta(\delta, \lambda)$. First, the index of refraction, and therefore the birefringence, of any material is not constant across the visible spectrum but exhibits dispersion. Thus, the actual retardance δ of any point in a thin section will in fact be different at different wavelengths of light. To account for this, the retardance was modeled linearly:

$$\delta = \delta_0 + a * (\lambda - \lambda_0)$$

where δ_0 is the retardance at wavelength λ_0 . λ_0 may be chosen to be any one of the sample wavelengths, and δ_0 and a are calculated to define a linear approximation to the retardance across the visible range. For materials with normal dispersion, birefringence will decrease as wavelength increases, so only negative values of a are considered.

The second difficulty that arises is due to the semi-periodic nature of $\Delta(\delta, \lambda)$. A plot of Δ as a function of λ for $\delta = 1000\text{nm}$, $a = 0.1$ is shown in Figure 2. This semi-periodic behavior means that there will inherently be multiple minima in parameter space when fitting to $\Delta(\delta, \lambda)$, and the best fit may

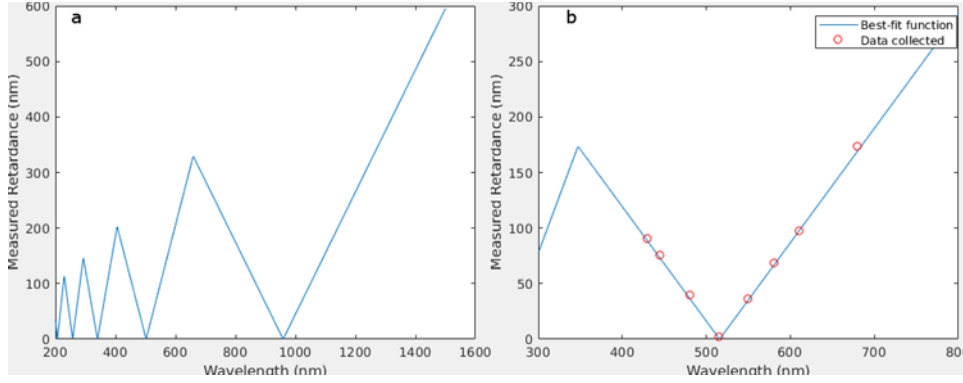


Figure 2: (a) Plot of equation (11), measured retardance Δ , as a function of wavelength λ , for the actual retardance $\delta_0 = 1000$ nm at $\lambda_0 = 550$ nm and $a = 0.1$. (b) Calculated retardance Δ for eight wavelengths at one pixel, along with the calculated best-fit for the data, using equation 11, which yields fit parameter values: $\delta_0 = 513$ nm $a = 0.03$.

depend on the initial conditions chosen. Therefore, a wide range of parameter space must be tested. To do this, the residue is calculated at many points in parameter space across a large range, and the minimum of these is used as the initial guess for fitting to $\Delta(\delta, \lambda)$. It should be noted that this process is computationally taxing especially considering that the fitting procedure must be done for $\sim 10^6$ pixels in each image. However, most images can be processed in under an hour using a standard personal computer. Once the retardance of each pixel has been calculated, the orientation of pixels that have a retardance δ for which $\frac{\lambda}{2} < \delta(\text{mod}\lambda) < \lambda$ is adjusted by $\frac{\pi}{2}$ according to equation (10).

C. EXAMPLE ARAGONITE DATA USING MPS, AND COMPARISON WITH OTHER METHODS

In this section, results from multiple aragonite samples are shown. MPS, as mentioned above, works on the assumption of a uniaxial sample. While aragonite is in fact biaxial, the index of refraction along the a- and b-axes are only different by .003-.005, and the birefringence between the c-axis and the a- or b-axis is .156, so aragonite can be treated as approximately uniaxial, with the c-axis being the fast axis and the slow axis being perpendicular to the c-axis. The samples include a geologic aragonite sample made up of a single crystal, a synthetic aragonite (SA) spherulite grown in the lab using the ammonium-carbonate diffusion method (Addadi et. al., 1987), and a coral skeleton (*Stylophora pistillata*) sample. A spherulite is a polycrystalline sphere in which a preferred axis of each crystallite (the c-axis in aragonite) is oriented along the radial direction. The *S. pistillata* skeleton was found to grow spherulitically in a previous study, in the form of a plumose spherulite, where the crystallites emanate in a fan or plume

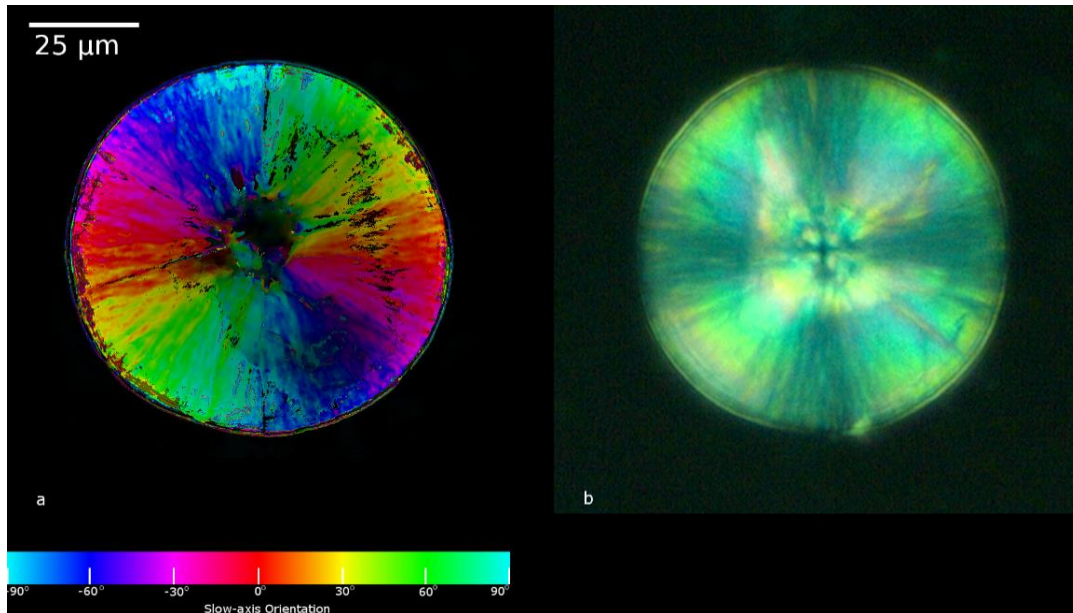


Figure 3: Synthetic aragonite (SA) spherulite in (a) imaged with the Multi-wavelength PolScope (MPS) developed here, where the full brightness colors indicate a maximum retardance of 1100 nm, and black a zero retardance. (b) The same SA spherulite imaged in reflected light with crossed polarizers. The c-axis (the fast axis in aragonite) is oriented in the radial direction in a spherulite, which is demonstrated by the Maltese cross visible in crossed polarizer images (such as b) and confirmed by the quantitative slow-axis measurement with the MPS in a.

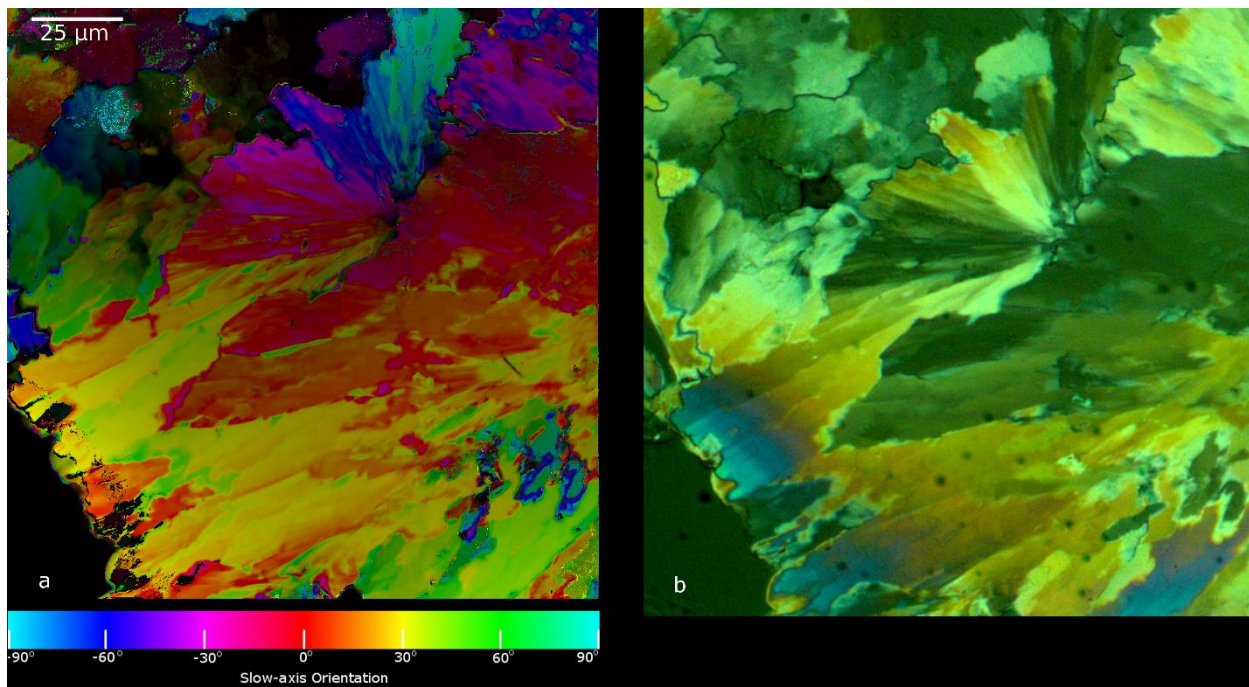


Figure 4: *Stylophora pistillata* coral skeleton. (a) The coral skeleton is imaged with MPS, with a maximum retardance of 750 nm. (b) The same region imaged in reflected light with crossed polarizers. It has been demonstrated that *S. pistillata* skeleton grows its skeleton spherulitically (Sun et. al., 2017); accordingly, we

would expect the c-axis to be oriented along the acicular crystallites, which emanate from the center of the fan-shaped structure, termed a plumose spherulite, in the center of the image.

shape instead of from a point (Sun et. al., 2017). Figures 3-6 show the orientation and retardance information in a composite colormap. The hue represents the in-plane slow-axis orientation measured from vertical, as indicated by the colorbar, and brightness represents retardance, with black being zero retardance, and fully saturated color being a maximum retardance specified for each image. Separate grayscale images for retardance and orientation can be found in Appendix II. All samples were prepared by embedding in EpoFix epoxy, grinding to the desired image plane, gluing to a glass slide, and grinding and polishing to a thickness of 5-15 μm .

Figures 3 and 4 include samples imaged with the MPS method and under crossed polarizers for comparison. In addition, Figure 5 shows two orientation maps of a *Stylophora pistillata* skeleton, one acquired with the MPS method, and one acquired with Polarization-dependent Imaging Contrast (PIC) mapping. PIC mapping is a technique that uses the linear dichroism of K- or L-edge absorption peaks of calcium or oxygen to image the orientation of the c-axis in carbonates through Photo-Emission Electron Microscopy (PEEM) (DeVol et. al., 2014). Using PEEM, one can achieve superior resolution, and only the surface of a sample is imaged, which highlights some of the limitations of imaging orientation using the MPS method. First, the resolution of the LC-PolScope is by nature the same as any visual light microscope, $\sim 200\text{-}300\text{nm}$ depending on the optics used. Second, imaging a thin section in transmitted light produces a few problems for the MPS method. When the crystallites in a polycrystalline material are small enough to include more than one in the thickness of a section, or at the edge where two crystallites overlap in the section, the light path will include multiple crystals. This will cause scattering, reducing the sharpness of the image around the edge where two crystallites overlap. This effect can be observed in Figure 5. Because PIC mapping is only sensitive to the surface of a sample, the edges of crystal domains appear far sharper when imaged with PIC mapping than when imaged in thin section with the LC-PolScope. In addition, if the light path includes multiple crystals within the thickness of the section, the path difference between the slow-axis and fast-axis polarization will be a result of the superposition of the crystals, not any one of them, causing the calculated slow-axis orientation and retardance to be a superposition of the orientations and the retardances of the crystals in the light path.

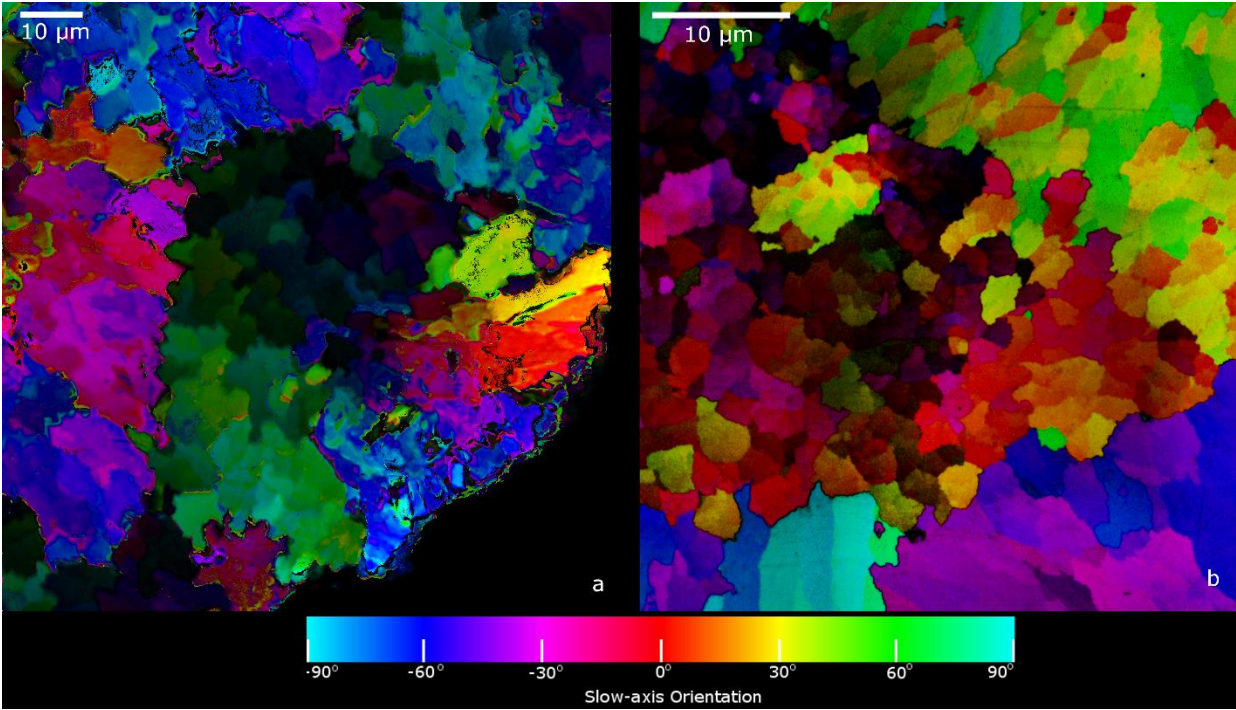


Figure 5: *S. pistillata* skeleton (a) Imaged with MPS, with maximum retardance of 750nm. (b) A similar area imaged with PIC mapping. The hue has been calibrated the same for both (a) and (b), but the brightness in a PIC map is directly proportional to the angle of the c-axis with the polarization plane.

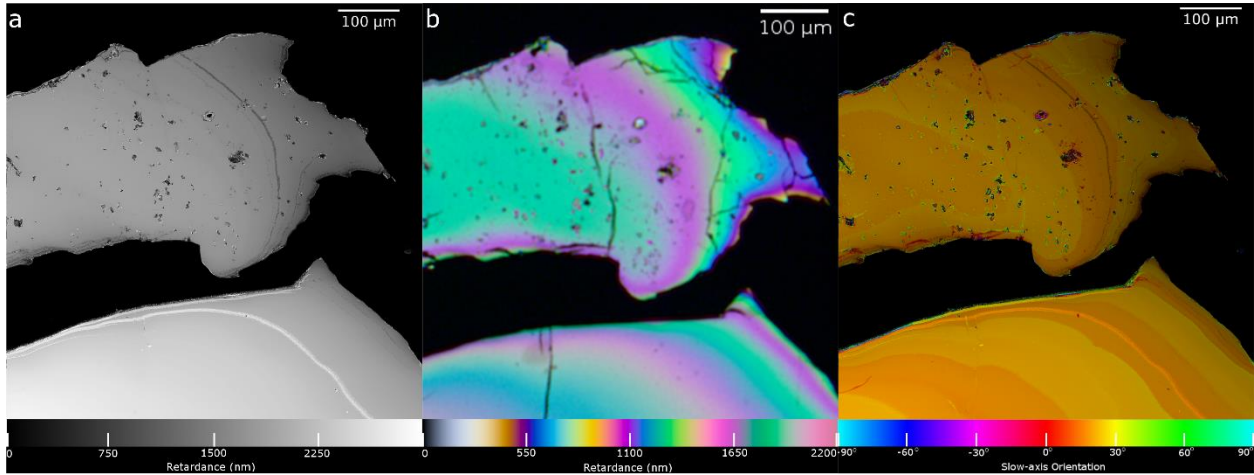


Figure 6: (a) and (c) Single crystal geologic aragonite sample imaged with MPS with a maximum retardance of 3 μ m. (b) Same sample imaged under crossed polarizers in transmitted light. (a) is a grayscale image mapping only retardance. When imaged in transmitted light, a thin section's retardance may be evaluated by comparing the interference colors with the Michel-Levy chart, a cross section of which is displayed in (b). By carefully comparing interference colors we can see that the minimum retardance of the sample is about 700-800 nm near the edge of the sample, continuously increasing past the maximum of the Michel-Levy chart in the thicker part of the sample. This matches well with the retardance calculated by MPS in (a). In (c) we observe that the multi-wavelength orientation calculation exhibits small 1-3 degree systematic errors.

We can observe this effect in Figure 4; near the edge of the sample (bottom left), large crystallites visible in the reflected light micrograph show correspondingly homogeneous orientation domains in the MPS image. However, in the plumose spherulite (top, middle) the crystallites visible in the reflected light micrograph are small enough that multiple crystallites may be stacked in the thickness of the section. In the MPS image the domains visible in the reflected light micrograph are indeed much less defined in this region, indicating that light is scattering through multiple crystals in this region. Thus, even though the MPS technique eliminates the low-retardance requirement for the LC-PolScope, for polycrystalline samples it is still desirable to have the section as thin as possible to help eliminate scattering within the section.

Figure 6 shows a single crystal geologic aragonite sample imaged with the LC-PolScope and in transmitted light under crossed polarizers. Using transmitted light allows use of the Michel-Levy interference chart to evaluate the retardance of the sample, which shows good agreement with the calculated retardance using the LC-PolScope. In addition, using a single crystal allows us to evaluate the precision of the orientation calculation of the MPS method. Figure 6(c) shows small, periodic 1-3 degree fluctuations in the calculated orientation. These alternating regions correspond to regions where the retardance is between $n\lambda$ and $(n + \frac{1}{2})\lambda$ and regions where the retardance is between $(n + \frac{1}{2})\lambda$ and $(n + 1)\lambda$ respectively. The orientation of pixels in the latter regions have been adjusted according to equation (10) and are slightly different than the orientation of pixels that have not been altered, even though the orientation of the single crystal should be uniform across the image. This shows a 1-3 degree systematic error in the orientation calculation.

Although PIC mapping has far better resolution than the MPS, taking data for PIC mapping requires use of a synchrotron x-ray source. Therefore, the PolScope, whose instrumentation is a transmitted light microscope with the liquid crystal retarder, is far more accessible and easy to use. In addition, the information given by both techniques is very similar. PIC mapping accurately images both the in-plane c-axis orientation and the angle of the c-axis from the polarization plane. In aragonite, the c-axis is the fast axis (in the uniaxial approximation), and thus is always perpendicular to the slow-axis. Therefore, measuring the in-plane slow-axis orientation, as the LC-PolScope does, is equivalent to measuring the in-plane c-axis orientation. In addition, since the retardance is a product of thickness and birefringence, it is theoretically possible to extract the angle of the c-axis from the image plane given the calculated retardance and some information about the thickness of the sample, although this is not attempted here (Oldenbourg, 2008). Both the PolScope and PIC mapping use the uniaxial approximation, which

means the a- and b-axis of aragonite, and any other approximately uniaxial mineral, are indistinguishable.

Another technique that is used to quantitatively measure crystal orientation at the micro-scale is Electron Backscatter Diffraction (EBSD). This is a Scanning Electron Microscope (SEM) technique that uses backscattered electron patterns (Kikuchi patterns) to measure crystal structure and orientation. Unlike PIC mapping and the LC-PolScope, EBSD does not work in the uniaxial approximation and can be used to find the full 3d orientation of a crystal- the a-, b-, and c-axis orientation. Similar to PIC mapping, EBSD is also only sensitive to the surface of a sample. However, the resolution is usually limited to a range similar to a visual light microscope. In addition, EBSD takes data one point at a time, so higher resolution images take longer- one image can take many hours to acquire data for. EBSD also requires a highly polished surface, which can be difficult to prepare. Thus, while each method has its own advantages and disadvantages, the MPS method provides a fast and accessible alternative to EBSD and PIC mapping for crystal orientation analysis of carbonates and other minerals at the micro-scale.

CRYSTAL ORIENTATION ANALYSIS OF OOIDS AT THE MICROSCALE

Using the MPS method and PIC mapping, two methods of crystal orientation mapping described in the previous section, I have done a detailed analysis of the crystal orientation structure of ooids at the microscale, with the goal of providing insights about their formation. However, in order to fully understand these results, it is necessary to interpret them through the lens of the many previous SEM studies of ooids, which have thoroughly documented the morphology of ooid cortices at the micro- and nanoscale.

A. BACKGROUND OF OOID MICROSTRUCTURE AND FORMATION

The primary structure of a tangential ooid is that of a nucleus surrounded by an aragonite cortex. The nucleus is a small grain or aggregate of mud or sand, and sometimes a small shell fragment. Around this nucleus are concentric laminae of aragonite 1-3 μm in thickness, which constitute the cortex (Simone, 1980). There can be anywhere from one single lamina forming the cortex to tens or over a hundred laminae. From thin sections viewed under crossed polarizers, it is easily deduced that the c-axis of aragonite is tangentially oriented with respect to these laminae (Sorby 1879, also see Figure 7). Separating the laminae are layers of organic matter, or sometimes empty space. Diaz et. al. (2017) studied in detail the different types of Extra-cellular Polymeric Substances (EPS), bacteria, and other organic matter in these layers of organic matter. SEM studies have determined that the microstructure

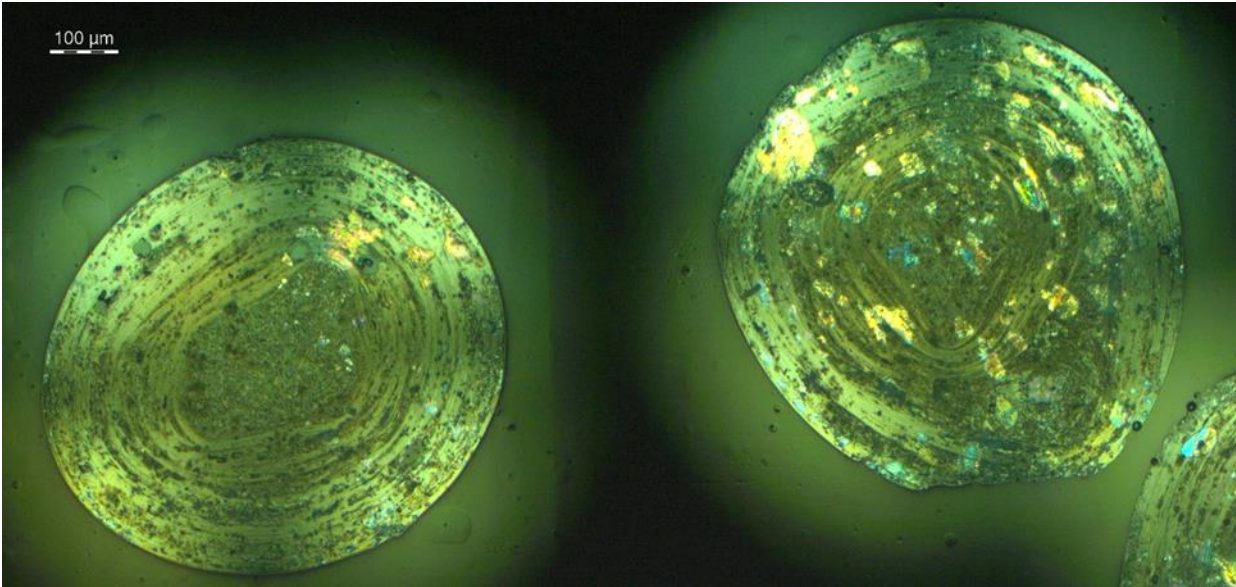


Figure 7: Reflected light micrograph of ooids in thin section under crossed polarizers. Same ooids as imaged with LC-PolScope in Figure 7 and 8.

of aragonite laminae consists primarily of three morphologies: (1) rods or batons on the order of 1-2 μm long and 100nm in diameter, with rounded ends- the most common morphology, (2) roughly spherical nanograins or balls 100-200nm in diameter, and (3) needles with similar dimensions as the batons, but with pointed ends (Loreau & Purser 1973, Fabricius 1977, Folk 1993, Folk & Lynch 2001). It was noted by Folk & Lynch (2001) and Duguid et. al. (2010) that the diameter of the balls is the same as the diameter of the batons, and it is likely nanoballs are simply rods that have not had the chance to develop. It is assumed by all authors that the c-axis is oriented along the long dimension of rods and needles, which seems likely given the growth anisotropy of aragonite along the c-axis. Since the nanograins are too small to be imaged in thin section, and PIC mapping is not sensitive to topography, making it impossible to tell sectioned batons from balls, and batons are the most commonly observed morphology, this study will focus mainly on batons. These batons are observed to be approximately tangential to the ooid lamina, but randomly oriented in the tangential surface (Loreau & Purser 1973). Loreau & Purser (1973) used this distribution of batons to explain the abnormally low birefringence of ooids in thin section.

Over the years, a few different theories of formation have been discussed. An important distinction is made between purely inorganic theories, and those that posit the influence or necessity of organic matter in ooid formation. The earliest theory of attributed ooid formation to a snowball effect (Sorby 1879), where small crystals of aragonite precipitated in waters supersaturated with respect to aragonite are mechanically aggregated by the ooid. However, it is not clear what the mechanism for adhesion would be. Many authors have also contended that the unique turbulent conditions of ooid

formation give rise to their unique structure; through frequent collisions between grains, growth of radially oriented needles is prevented (Davies et. al. 1978, Loreau & Purser 1973, Diaz et. al. 2017). Davies et. al. (1978) grew ooids in the lab with the characteristic tangential baton structure by balancing the conditions of agitation of grains without any organic material introduced. However, the of quiet-water ooids from Bimini lagoon studied by Bathurst (1967) provide an important counter-example to this theory. The movement of ooids in Bimini lagoon is restricted by algae, and the quiet conditions of the lagoon. However, ooids are found that consist of a thin 2-3 μ m cortex made of only one lamina, which is identical to the laminae found in ooids formed in high-energy environments. This suggests that turbulence is not necessary for the characteristic tangential baton structure of ooid cortices, but their periodic movement does play a role in the periodic growth of laminae. Other authors give more importance to the presence of organic material, either as a substrate for periodic crystal growth (Diaz et. al., 2017), as actively contributing to conditions that favor crystal growth (Mitterer, 1989), or by the biomineralization of bacteria (Folk & Lynch, 2001).

Most notable in recent studies is the presence of amorphous calcium carbonate (ACC) in ooids. ACC has been observed to be formed by calcifying algae and EPS from bacteria in environments similar to those of ooid growth. Diaz et. al. (2017) were the first to find direct evidence of ACC, and argued for a model of ooid growth where each concentric lamina is formed by a layer of ACC precipitated in EPS while in a resting stage of the ooid, which later crystallizes. Duguid et. al. (2010) also found indirect evidence for ACC through magnesium concentrations of forming ooid cortices, though they argued for an abiotic origin. The discovery of ACC in ooids may also explain the observation of previous authors of a thin 'mucus' that often forms a thin coat around ooids (Loreau & Purser, 1973).

B. RESULTS

Figures 8 and 9 show MPS images of two ooids, quantitatively confirming the characteristic tangential orientation of ooid cortices, which display almost perfectly tangential orientation at every point. The resolution using the LC-PolScope was not sufficient to resolve individual baton crystallites, and in addition the measured orientation and retardance are likely a superposition of many crystals within the thickness of the section. However, in Figure 11 individual laminae are clearly visible, with a thickness of $1.3 \pm 0.5 \mu\text{m}$, in agreement with past measurements. See Table 1 for measurement results.

Figures 10 and 11 show PIC maps of three separate sections of ooid cortices on two ooids. Here baton crystallites are clearly visible. Also prominent are smaller circular particles or dots, however since PIC mapping requires a highly polished surface it is not sensitive to topography and therefore it is

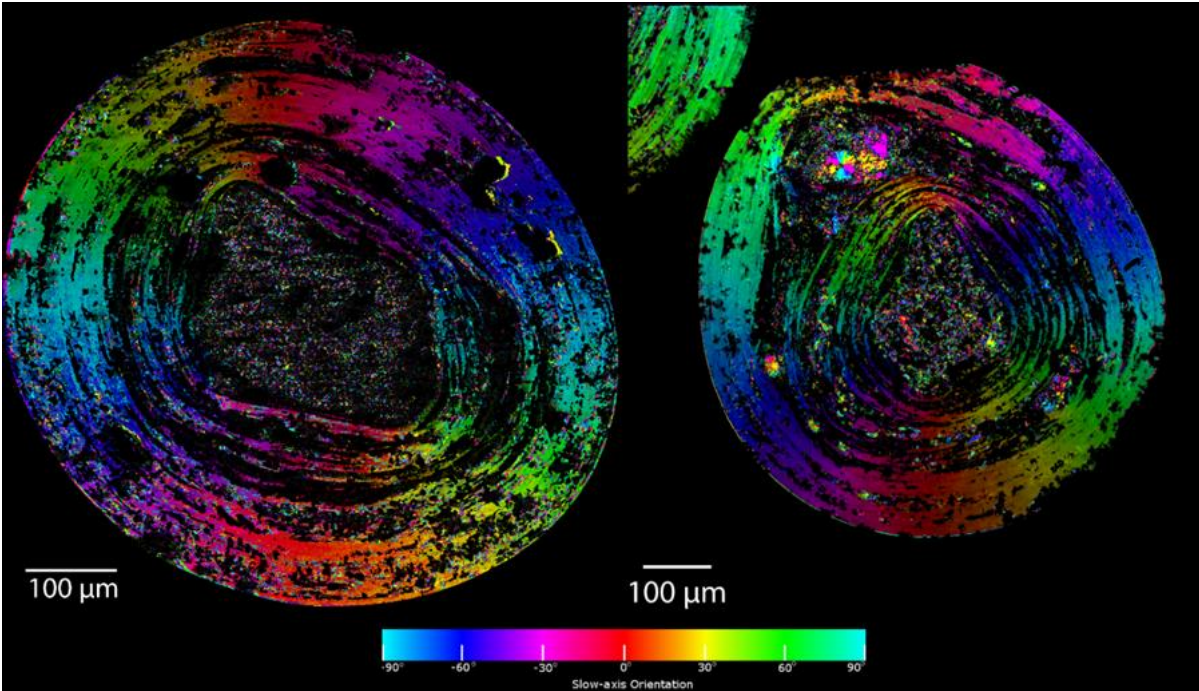


Figure 8: Two whole ooids imaged with MPS, maximum retardance 300nm. Areas of low transmission (layers with organic material and/or micritization) were masked out. Most individual laminae are too small to be resolved at this magnification. Many microborings are visible, ranging in size from 2.5-20 μ m. Most notable is the continuous distribution of orientations; even on the innermost laminae the orientation is tangential at every point, with no visible orientation boundaries.

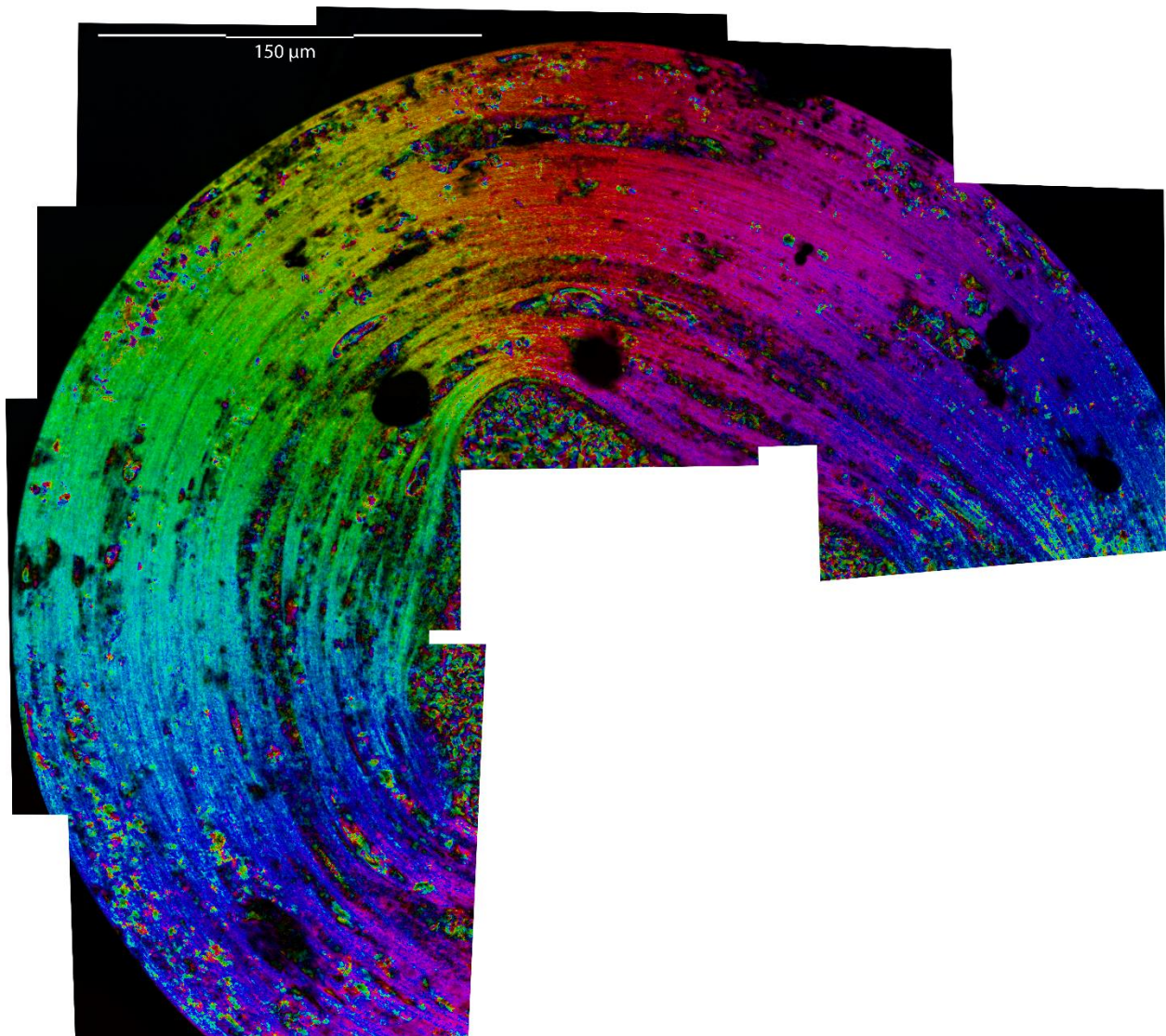


Figure 9: Composite image showing detail of the cortex of the first ooid imaged in Figures 7 and 8. Individual laminae are clearly visible, and have thicknesses of $1.3 \pm 0.5 \mu\text{m}$. Although individual orientation domains are visible, after closer examination they are close to the diffraction limit of the system, and are not likely to be visible individual crystals, and the orientations observed are still likely to be a superposition of many rods in the thickness of the section.

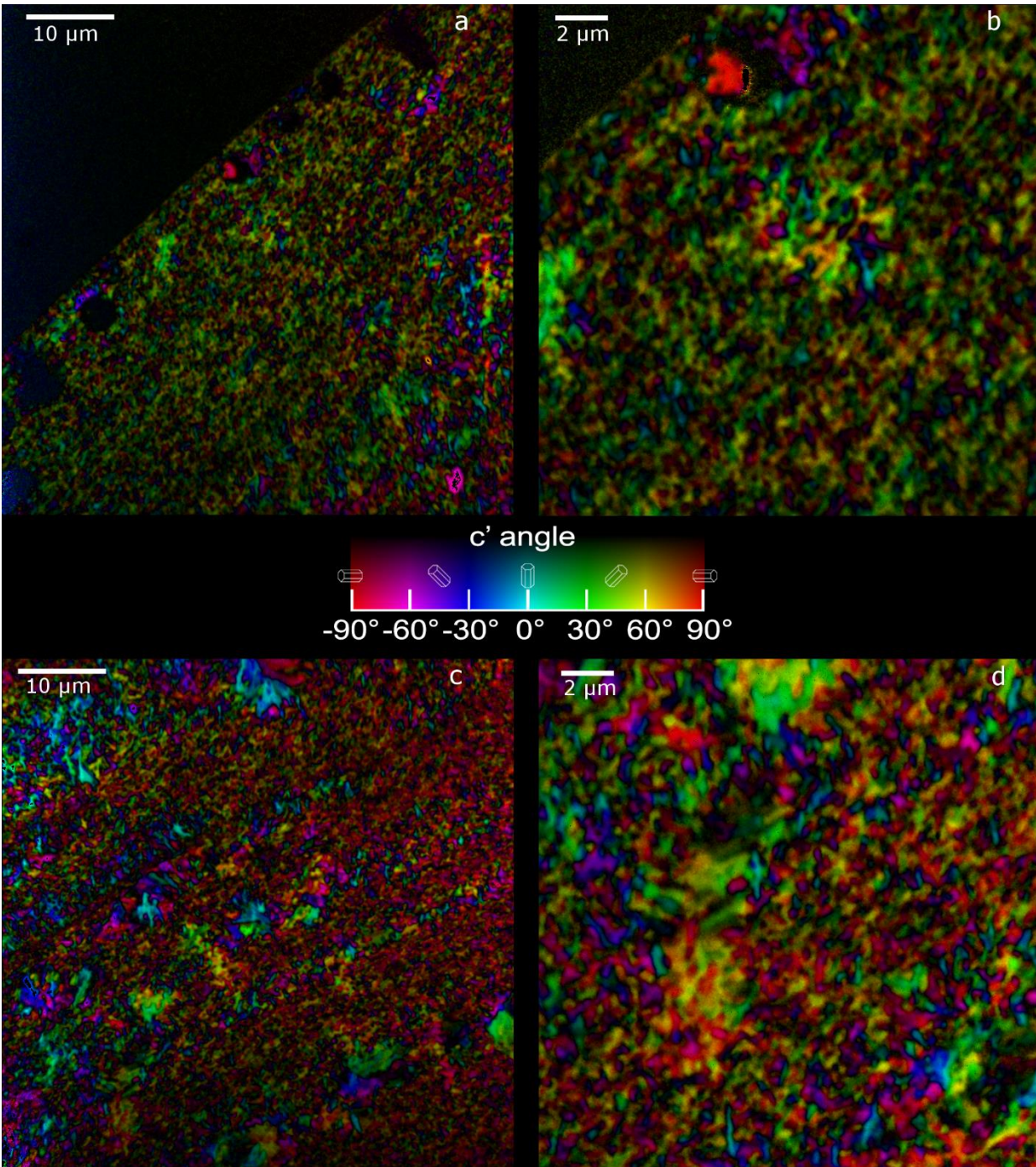


Figure 10: PIC maps of two separate areas in an ooid cortex, with a large field of view (60 μ m, a & c), and small field of view (20 μ m, b & d). The primary morphology is of small rods and dots, which can be interpreted as rods pointing out of the image plane. However, especially in the bottom images, there are some larger crystal domains. The primary crystal orientations are approximately tangential, but all orientations are present, even though only a small angular slice of the ooid is shown.

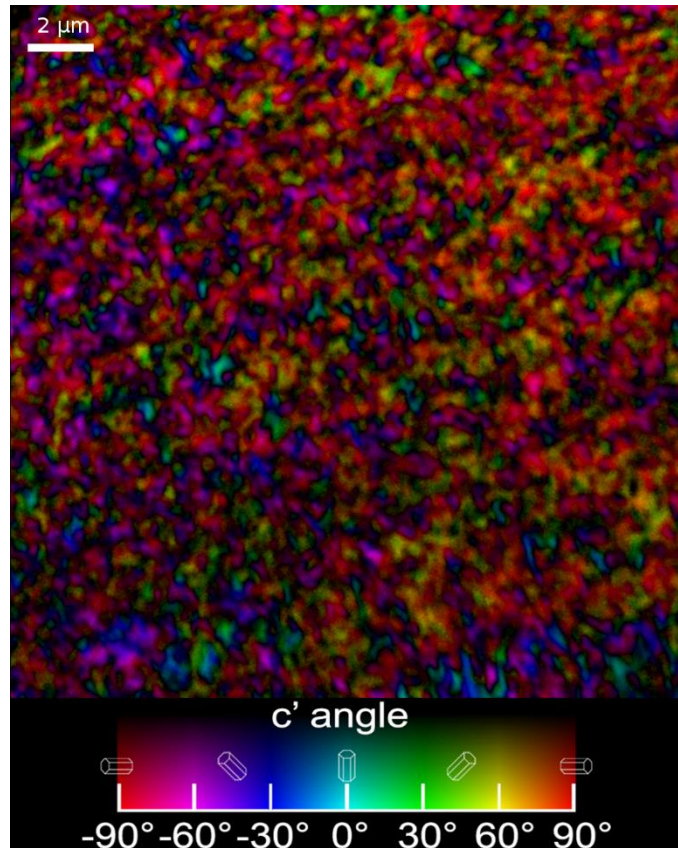


Figure 11: PIC map of a third region in an ooid cortex, showing especially homogeneous distribution of particle shapes and sizes.

impossible to tell whether these dots are nanograins as observed by Folk (1993), or batons which are pointed out of the image plane. Due to the prominence of rods in ooid cortices over nanograins, it is safe to assume most dots observed in PIC mapping are rods pointing out of the image plane. This is confirmed by the fact that in most cases the batons visible in Figure 10 are brighter than surrounding dots, indicating their c-axes are more in-plane. The size of particles visible in PIC mapping was measured by measuring the length of their longest dimension. The longest particles were 1.5 μm in length, and the smallest was 160nm in length (see Appendix II and Table 2). If dots are to be interpreted as sectioned rods, then the length of the smallest particles will correspond to the diameter of rods. This means our minimum length of 160nm corresponds to the diameter of rods, which agrees well with the 100-200nm range given by others (Folk & Lynch 2001). In addition, the longest particles will be the rods oriented most in-plane, so our length maximum of 1.5 μm can be interpreted as roughly the length of rods in the ooids sectioned. This corresponds well to the 1-2 μm measurements of other authors (Loreau & Purser 1973, Folk & Lynch 2001). In addition to the rods and dots, there are occasional regions of larger crystal domains. These regions are irregular in shape, and hard to interpret. Some could be interpreted as

bundles of closely co-oriented needles, as observed in Folk & Lynch (2001), but the fact that these regions often diverge the most from tangential orientation suggests they may be recrystallized regions inside micro-borings. This is supported by a large crystal domain visible in Figure 10(a & b), which is clearly forming in a micro-boring hole.

While the primary orientation is tangential, all orientations are visible in each PIC map even though only a small angular slice of the cortex is visible. Though it was not possible to tell which ooid was being imaged in PEEM because there were many ooids embedded in the sample and the field of view of PEEM is too small to identify large-scale features, the average diameter of the ooids embedded was $533 \pm 46\mu\text{m}$, or an average circumference of $1.67 \pm 0.14\text{mm}$ (see Appendix II and Table 3). Therefore, a $60\mu\text{m}$ field of view can only encompass a 12° angular portion of an ooid, and a $20\mu\text{m}$ field of view can only encompass a 4° angular section of an ooid. Thus, the presence of all orientations in PIC maps suggests not only a significant deviation from tangential orientation, but that some crystallites are randomly oriented. To assess this claim, the distribution of crystal orientations in the PIC maps of ooid cortices was analyzed. Figure 12 shows that, while the distribution of orientations is a poor fit to a truncated normal distribution (truncated because crystal orientations are only allowed in a 180° range), it is a good fit to a Gaussian shifted by a constant:

$$N(x) = A \cdot e^{-\frac{(x-\mu)^2}{2\sigma^2}} + C$$

where $N(x)$ is the number of pixels oriented at x degrees, σ is the standard deviation, and μ is the mean of the Gaussian. This suggests that a certain percentage of crystallites in the cortex ($\frac{C\pi}{\int_{-\pi}^{\pi} N(x)dx}$) are randomly oriented while the rest have an orientation correlated with the tangential direction. For Figure 11 the percentage of random orientations is 31.5%. Figure 11 is an exemplary case where no large blocky crystal domains are present that may be recrystallized micro-borings. For Figure 10(c), where there are many of these regions, the calculated proportion of random orientations is 51.8%. Other calculated proportions of random orientations were, for Figure 10(a) 33.0%, Figure 10(b) 24.4%, and for a small slice of Figure 10(a), 21.7%. This shows that a significant number of crystallites (at least 20%), have no correlation to the tangential direction. In addition, the standard deviation σ of crystal orientations was $18\text{-}20^\circ$ regardless of the field of view. Finally, the average orientation was shown to differ significantly from the tangential direction. In Figure 10(a), where the tangential direction can be measured unambiguously to be -48° from vertical, the average orientation is -60.1° from vertical. Details

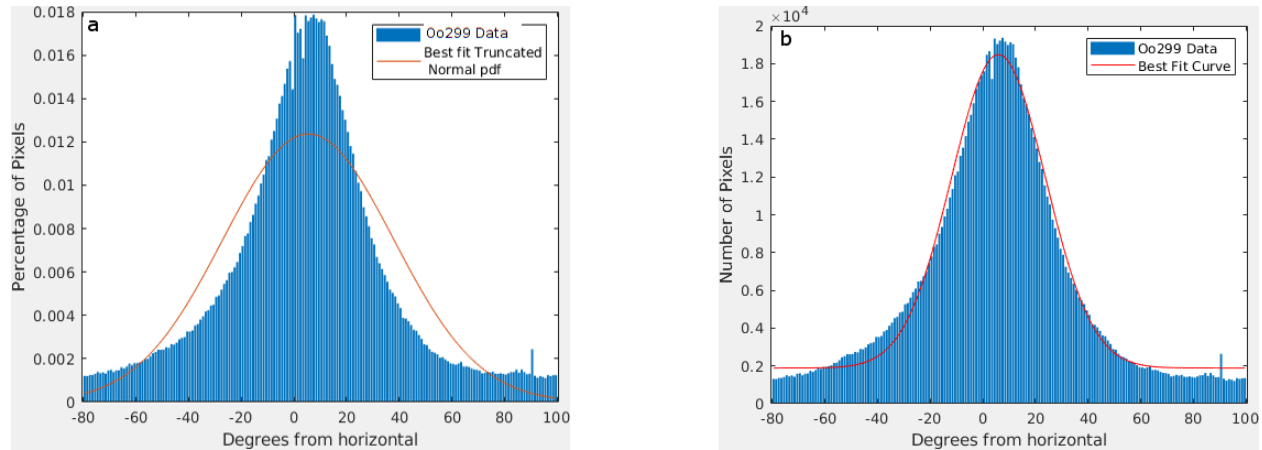


Figure 12: Orientation distribution of pixels in Figure 10(b). (a) Fit to truncated normal distributions. (b) Fit to shifted Gaussian $A \cdot e^{-\frac{(x-\mu)^2}{2\sigma^2}} + C$ ($\sigma = 17.9, \mu = 5.92, A = 16,590, C = 1891$).

of lamina thickness, particle size, and ooid circumference calculations can be found in Appendix II and Tables 1-3.

C. DISCUSSION

First, it should be noted that the observations above largely confirm the observations of Loreau & Purser (1973), who measured the microstructure of ooid cortices with SEM and TEM, noting the large deviation of rods from tangential and confirming that the c-axis is along the long axis of the rods with TEM. However, having bulk information about crystal distribution in ooid cortices allows for some concrete conclusions about ooid formation.

Using the MPS method, the orientation of ooid cortices was measured as perfectly tangential at each point. While PIC mapping shows that this is an aggregate effect of approximately tangentially aligned crystallites, it is an important indication that crystal growth is homogeneous around the ooid cortex on the scale of the whole ooid. The question that must be addressed is how this remarkably homogeneous tangential structure is achieved. As discussed above, the most prevalent theory is that crystallites start growing with random orientation, but the more radially oriented they are, the more likely they are to be broken off by grain-to-grain contacts in turbulent conditions. However, the data above show a significant portion of crystallite orientations have no correlation whatsoever with the tangential direction. In the turbulence-mediated model, this would be equivalent to some fraction of crystallites being protected from abrasion, which seems unlikely. What these crystallites that are uncorrelated with the tangential direction suggest instead is that ooid cortex growth begins with

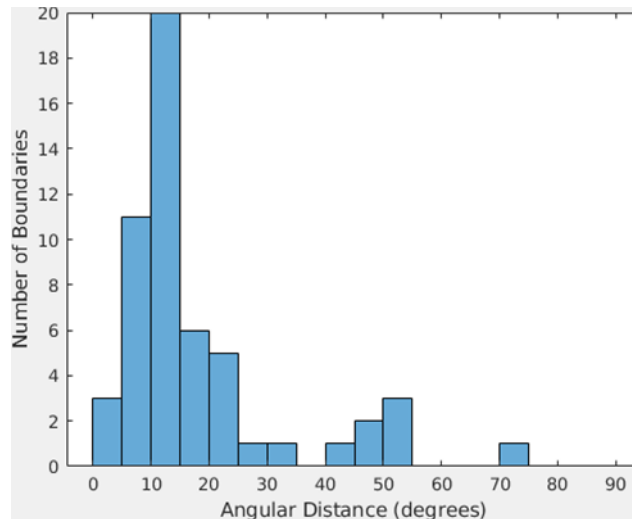


Figure 13: Histogram of angle boundaries between adjacent particles in Figure 10(b). Number of boundaries, n = 54. Details of angular distance measurement in Appendix II.

precipitation of randomly oriented crystallites, which constitute around 20% of the cortex lamina once it is done forming. It is also noted that the angle boundaries between neighboring crystallites are most often small. Figure 13 shows a histogram of measured angle boundaries between adjacent particles in Figure 10(b). The most likely angle boundary is 15-20°, suggesting non-crystallographic small angle branching. This type of crystal growth is observed in spherulitic growth, specifically the SA spherulite and *S. pistillata* skeleton (Sun et. al., 2017) shown in the previous section and is in fact necessary for it (Granasy et. al., 2005). Because aragonite grows fastest along its c-axis, this small-angle branching potentially allows a polycrystalline material to fill space in the most efficient way possible.

The model of formation that is most likely to produce the observations above is a model of ACC mediated growth. In this model, I propose that the tangential structure of ooids is mediated by space-filling instead of abrasion in the following way. (1) A thin layer of ACC forms on the outer layer of the ooid. This is observed directly by Diaz et. al (2017), who asserted ACC is precipitated via organomineralization of bacteria and algae, and indirectly by Duguid et. al. (2010) who claimed the outer layer of the cortex was ACC based on elevated Mg²⁺ levels, and asserted it was a product of water chemistry. (2) This layer then begins to crystallize. Crystallites are nucleated randomly, then grow and branch via small-angle branching. While crystallites oriented radially will quickly be stopped by the edge of the substrate (the ACC layer), those oriented more tangentially will be able to elongate and branch in the tangential plane, filling the substrate more efficiently. This allows for a small fraction of observed orientations, the originally nucleated ones, to be uncorrelated with the tangential direction, while still explaining the overall tangential orientation of the ooid cortex.

D. CONCLUSIONS

A detailed analysis of the crystal orientations of ooid cortices was performed. Unfortunately, due to the small size of crystallites that make up an ooid cortex, the MPS method was not able to resolve many small scale features, but did confirm the homogeneous (aggregate) tangential orientation of the ooid cortex. Using PIC mapping, it was possible to map the crystal orientations of particles identifiable with the rods and nanoballs previously identified in SEM studies. Through an analysis of the distribution of orientations in an ooid cortex, it was determined that about 20% of them have no correlation to the tangential direction, and that they frequently exhibit small-angle branching. Combined with the knowledge that ACC most likely plays a role in ooid formation, these results can be explained in terms of a new model, where crystal growth takes place inside a layer of ACC, and the efficiency of tangentially oriented crystallites in filling space within this layer determines the overall approximately tangential structure of the ooid cortex. Because the individual laminae and any areas of organic material were not discernable in PIC mapping, it was impossible to make any conclusion about whether the precipitation of ACC itself is biologically mediated in any way. Although this study suggests ACC precipitation is a primary or significant factor in ooid growth, more studies should be done on fresh ooids to assess the quantity and origin of ACC.

REFERENCES

- Addadi, L., Moradian, J., Shay, E., Maroudas, N.G. and Weiner, S., 1987. A chemical model for the cooperation of sulfates and carboxylates in calcite crystal nucleation: relevance to biomineralization. *Proceedings of the national academy of sciences*, 84(9), pp.2732-2736.
- Bathurst, R.G.C., 1967. Oölitic films on low energy carbonate sand grains, Bimini Lagoon, Bahamas. *Marine Geology*, 5(2), pp.89-109.
- Bragg, W.L., 1924. The refractive indices of calcite and aragonite. *Proceedings of the Royal Society of London. Series A*, 105(732), pp.370-386.
- Bragg, W.L. and Pippard, A.B., 1953. The form birefringence of macromolecules. *Acta Crystallographica*, 6(11-12), pp.865-867.
- Davies, P.J., Bubela, B. and Ferguson, J., 1978. The formation of ooids. *Sedimentology*, 25(5), pp.703-730.
- Duguid, S.M., Kyser, T.K., James, N.P. and Rankey, E.C., 2010. Microbes and ooids. *Journal of Sedimentary Research*, 80(3), pp.236-251.

DeVol, R.T., Metzler, R.A., Kabalah-Amitai, L., Pokroy, B., Politi, Y., Gal, A., Addadi, L., Weiner, S., Fernandez-Martinez, A., Demichelis, R. and Gale, J.D., 2014. Oxygen spectroscopy and polarization-dependent imaging contrast (PIC)-mapping of calcium carbonate minerals and biominerals. *The Journal of Physical Chemistry B*, 118(28), pp.8449-8457.

Diaz, M.R., Eberli, G.P., Blackwelder, P., Phillips, B. and Swart, P.K., 2017. Microbially mediated organomineralization in the formation of ooids. *Geology*, 45(9), pp.771-774.

Eder, M., Lütz-Meindl, U. and Weiss, I.M., 2010. Non-invasive LC-PolScope imaging of biominerals and cell wall anisotropy changes. *Protoplasma*, 246(1), pp.49-64.

Fabricius, F.H., 1977. Origin of marine ooids and grapestones. In: H. Fuchtbauer, A.P. Lisitzyn, J.D. Milliman, E. Seibold (Editors), *Contribution to Sedimentology*, 7. Schweizebart'sche Verlagsbuchhandlung, Stuttgart, pp. 1--113.

Franco, C., Britto, K., Wong, E., Hou, G., Zhu, S.N., Chen, M., Cybulsky, M.I. and Bendeck, M.P., 2009. Discoidin domain receptor 1 on bone marrow-derived cells promotes macrophage accumulation during atherogenesis. *Circulation research*, 105(11), pp.1141-1148.

Folk, R.L., 1993. SEM imaging of bacteria and nannobacteria in carbonate sediments and rocks. *Journal of Sedimentary Research*, 63(5).

Folk, R.L. and Lynch, L.F., 2001. Organic matter, putative nannobacteria and the formation of ooids and hardgrounds. *Sedimentology*, 48(2), pp.215-229.

Glazer, A.M., Lewis, J.G. and Kaminsky, W., 1996. An automatic optical imaging system for birefringent media. *Proc. R. Soc. Lond. A*, 452(1955), pp.2751-2765.

Heilbronner, R.P. and Pauli, C., 1993. Integrated spatial and orientation analysis of quartz c-axes by computer-aided microscopy. *Journal of Structural Geology*, 15(3-5), pp.369-382.

Keikhosravi, A., Eliceiri, K.W. and Liu, Y., 2018, March. PolScope based imaging and quantification of fibrillar collagen organization (Conference Presentation). In *Three-Dimensional and Multidimensional Microscopy: Image Acquisition and Processing XXV* (Vol. 10499, p. 104990Q). International Society for Optics and Photonics.

Loreau, J.P. and Purser, B.H., 1973. Distribution and ultrastructure of Holocene ooids in the Persian Gulf. In *The Persian Gulf* (pp. 279-328). Springer, Berlin, Heidelberg.

Maitland, D.J. and Walsh, J.T., 1997. Quantitative measurements of linear birefringence during heating of native collagen. *Lasers in surgery and medicine*, 20(3), pp.310-318.

Mitterer, R.M., 1989. Composition and association of organic matter with calcium carbonate and the origin of calcification. In *Origin, evolution, and modern aspects of biomineralization in plants and animals* (pp. 309-323). Springer, Boston, MA.

Oldenbourg, R. and Mei, G., 1995. New polarized light microscope with precision universal compensator. *Journal of microscopy*, 180(2), pp.140-147.

Oldenbourg, R., 2003. Polarization microscopy with the LC-PolScope.

Oldenbourg, R., 2008. Polarized light field microscopy: an analytical method using a microlens array to simultaneously capture both conoscopic and orthoscopic views of birefringent objects. *Journal of microscopy*, 231(3), pp.419-432.

Rosin, N.L., Agabalyan, N., Olsen, K., Martufi, G., Gabriel, V., Biernaskie, J. and Di Martino, E.S., 2016. Collagen structural alterations contribute to stiffening of tissue after split-thickness skin grafting. *Wound Repair and Regeneration*, 24(2), pp.263-274.

Shribak, M. and Oldenbourg, R., 2003. Techniques for fast and sensitive measurements of two-dimensional birefringence distributions. *Applied Optics*, 42(16), pp.3009-3017.

Simone, L., 1980. Ooids: a review. *Earth-Science Reviews*, 16, pp.319-355.

Sorby, H.C., 1879. The structure and origin of limestones. *The Popular science review*, 3(9), pp.134-137.

Vidal, B.C., 1970. Interferometric and histochemical investigation on collagen bundles: refractive indices and dry masses prior and after staining with orange G. In *Annales d'histochimie* (Vol. 15, No. 3, p. 191).

Volkmer, D., Harms, M., Gower, L. and Ziegler, A., 2005. Morphosynthesis of Nacre-Type Laminated CaCO₃ Thin Films and Coatings. *Angewandte Chemie International Edition*, 44(4), pp.639-644.

Appendix I: Derivation of Equations 10 and 11

April 30, 2018

1 Equation 10

We shall start with main text equations (6)

$$\phi = \begin{cases} \frac{1}{2} \text{atan2}(A, B) & \text{if } C \geq 0 \\ \frac{1}{2} \text{atan2}(-A, -B) & \text{if } C < 0 \end{cases} \quad (1)$$

and (9)

$$\theta = \begin{cases} \frac{1}{2} \text{atan2}(A, B) & \text{if } \tan(d) \geq 0 \\ \frac{1}{2} \text{atan2}(-A, -B) & \text{if } \tan(d) < 0 \end{cases} \quad (2)$$

where $d = 2\pi\delta/\lambda$, and $C = \cos(d)$ Now since $\tan(d) = \frac{\sin(d)}{\cos(d)}$, equations 1 and 2 agree if $\sin(d) \geq 0$, and we only have to consider the case that $\sin(d) < 0$. First consider that $(2n-1)\pi < d < (2n-1/2)\pi$, so that d is in Quadrant III. Then $C < 0$, but $\tan(d) > 0$, so

$$\phi = \frac{1}{2} \text{atan2}(-A, -B) \quad (3)$$

$$\theta = \frac{1}{2} \text{atan2}(A, B) \quad (4)$$

Supposing that $B > 0$, this means

$$\phi = \frac{1}{2} \left(\pi + \arctan\left(\frac{A}{B}\right) \right)$$

and

$$\theta = \frac{1}{2} \arctan\left(\frac{A}{B}\right) \Rightarrow$$

$$\theta = \phi - \frac{\pi}{2}$$

for $(2n-1)\pi < d < (2n-1/2)\pi$ and $B > 0$. Assuming instead that $B < 0$ means that

$$\theta = \frac{1}{2}(\pi + \arctan(\frac{A}{B}))$$

and

$$\begin{aligned} \phi &= \frac{1}{2}\arctan(\frac{A}{B}) \Rightarrow \\ \theta &= \phi + \frac{\pi}{2} \end{aligned}$$

Since crystal orientations are double-headed vectors, θ is equivalent modulo π , so that $\phi + \frac{\pi}{2} = \phi - \frac{\pi}{2}$. Similarly, if we consider that d is instead in Quadrant IV, the role of θ and ϕ in equation 3 and 4 simply switched, so we find that:

$$\theta(\phi, \delta, \lambda) = \begin{cases} \phi & \text{if } 0 < \delta(\text{mod } \lambda) < \frac{\lambda}{2} \\ \phi + \frac{\pi}{2} & \text{if } \frac{\lambda}{2} < \delta(\text{mod } \lambda) < \lambda \end{cases} \quad (5)$$

2 Equation 11

For equation 11, we begin with main text equation (5):

$$\Delta = \begin{cases} \frac{\lambda}{2\pi}(\arctan([A^2 + B^2]^{1/2})) & \text{if } C \geq 0 \\ \frac{\lambda}{2\pi}(\pi - \arctan([A^2 + B^2]^{1/2})) & \text{if } C < 0 \end{cases} \quad (6)$$

noting that $[A^2 + B^2]^{1/2} = |\tan(2\pi\delta/\lambda)|$. As mentioned in the text, using \arctan to calculate Δ , means that Δ can at best be accurate modulo λ . Thus, if $\sin(2\pi\delta/\lambda) \geq 0$,

$$\Delta = \delta \pmod{\lambda}$$

Now consider the case that $\sin(2\pi\delta/\lambda) < 0$. If $2\pi\delta/\lambda$ is in Quadrant III, $C < 0$, so $\Delta = \frac{\lambda}{2\pi}(\pi - \arctan([A^2 + B^2]^{1/2}))$. However, since both $\cos(2\pi\delta/\lambda)$ and $\sin(2\pi\delta/\lambda)$ are less than 0, $\tan(2\pi\delta/\lambda) > 0$, which means

$$\begin{aligned} \delta \pmod{\lambda} &= \frac{\lambda}{2\pi}(\pi + \arctan([A^2 + B^2]^{1/2})) \Rightarrow \\ \Delta &= \frac{\lambda}{2\pi}(2\pi - (\pi + \arctan([A^2 + B^2]^{1/2}))) = \lambda - \delta \pmod{\lambda} \end{aligned}$$

if $2\pi\delta/\lambda$ is in Quadrant III. Similarly, if $2\pi\delta/\lambda$ is in Quadrant IV, then, according to equation 6,

$$\Delta = \frac{\lambda}{2\pi}(\arctan([A^2 + B^2]^{1/2}))$$

but since $\tan(2\pi\delta/\lambda) < 0$, we know that

$$\delta \pmod{\lambda} = \frac{\lambda}{2\pi}(2\pi + \arctan(-[A^2 + B^2]^{1/2}))$$

Combining these results gives main text equation (11):

$$\Delta = \begin{cases} \delta \pmod{\lambda} & \text{if } 0 \leq 2\pi\delta/\lambda < \pi \\ \lambda - \delta \pmod{\lambda} & \text{otherwise} \end{cases} = (\delta \pmod{\lambda}) \wedge (\lambda - \delta \pmod{\lambda}) \quad (7)$$

APPENDIX II: SUPPLEMENTARY DATA

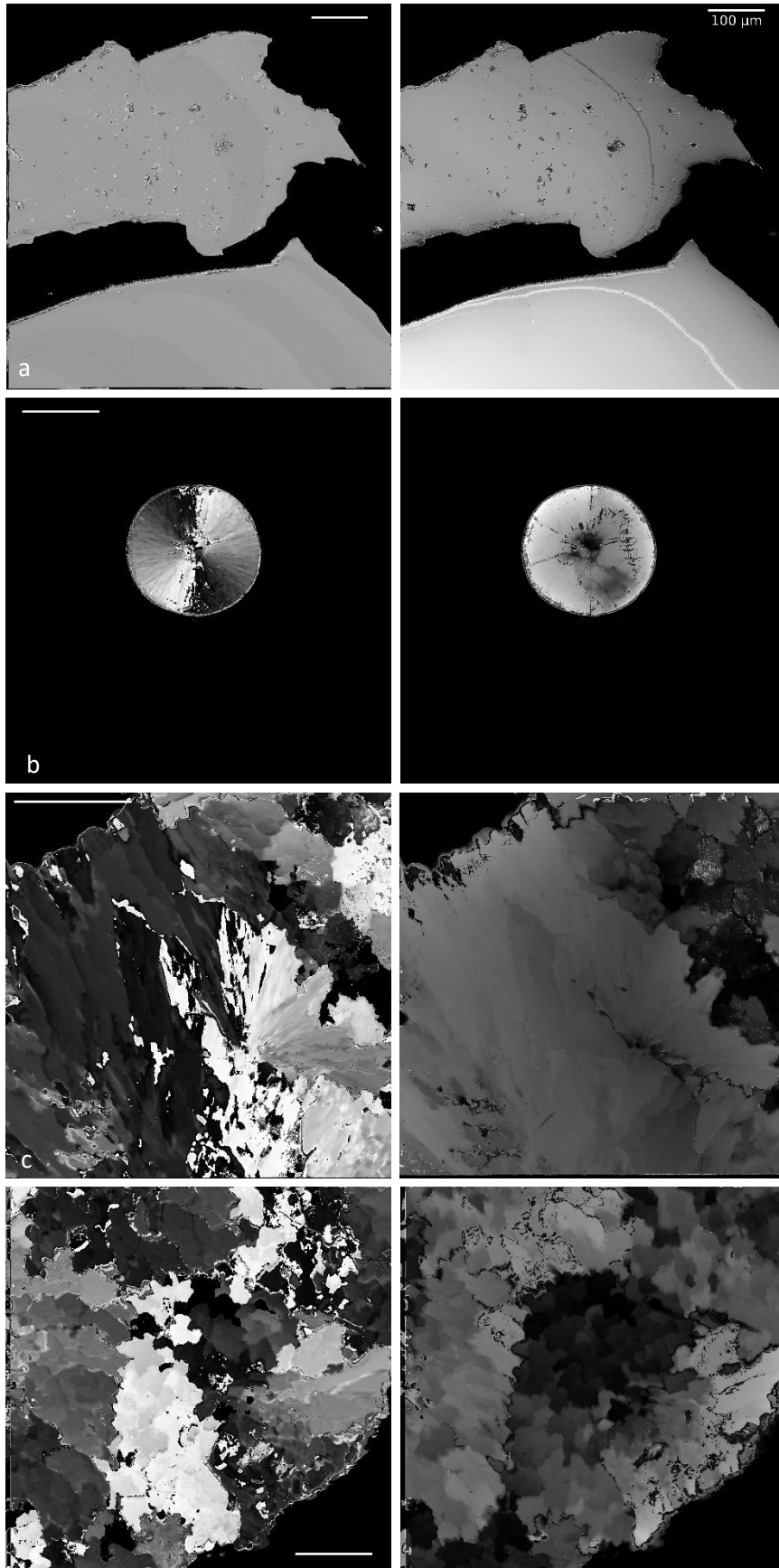
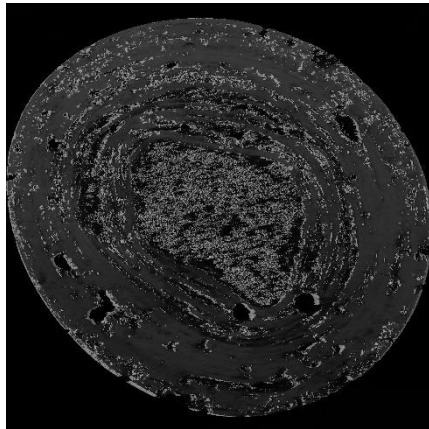
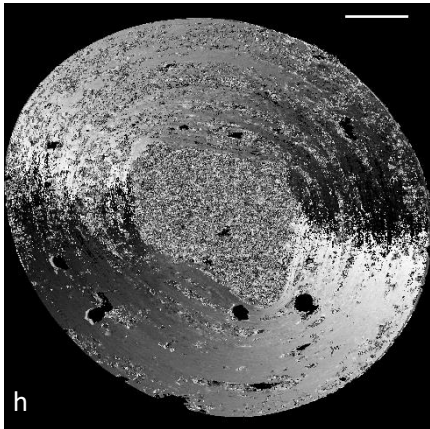
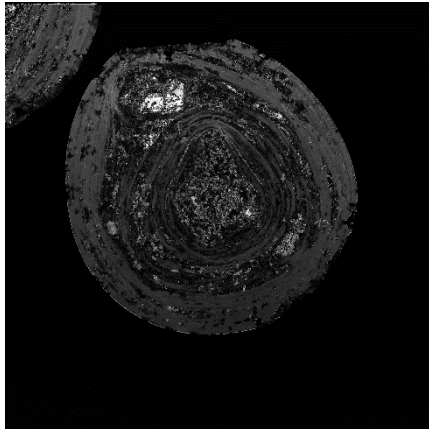
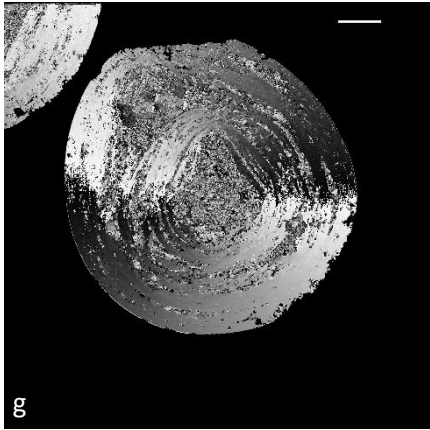
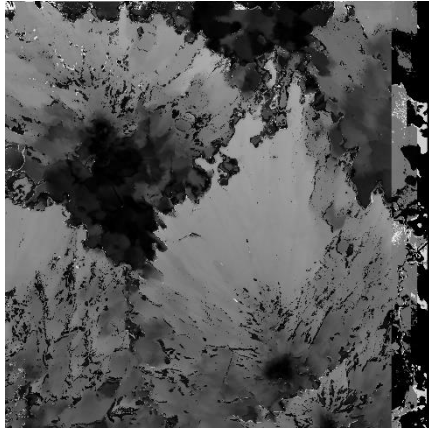
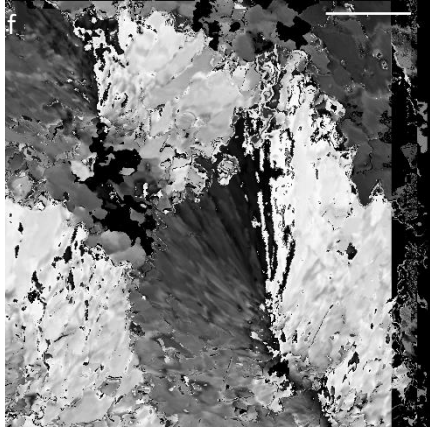
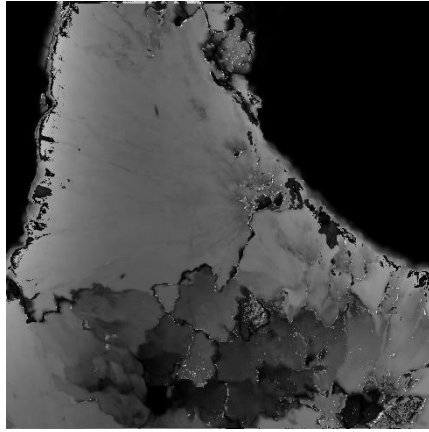
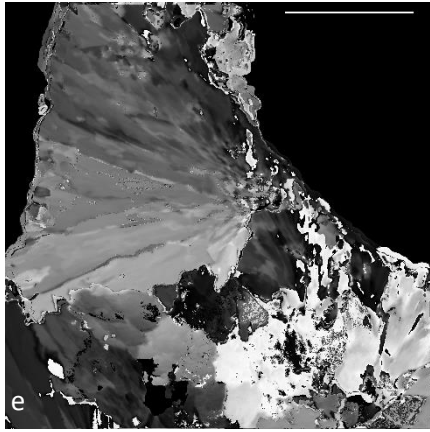


Figure A1: Grayscale orientation (right), and retardance (left) images. Orientation ranges from 0° from horizontal (black) to 180° (white). Retardance ranges from 0 (black) to specified maximum (white).

a) Geologic aragonite, maximum retardance $3\mu\text{m}$ b) SA spherulite, maximum retardance $1.1\mu\text{m}$ c-f) Coral skeleton (*S. pistillata*). Maximum retardance of $1.2\mu\text{m}$ for c) and d), $1\mu\text{m}$ for e), and $1.5\mu\text{m}$ for f). Scale bars are all $50\mu\text{m}$ except a), which is $100\mu\text{m}$.

g,h) Ooids, maximum retardance of $1\mu\text{m}$ and $1.5\mu\text{m}$ respectively.



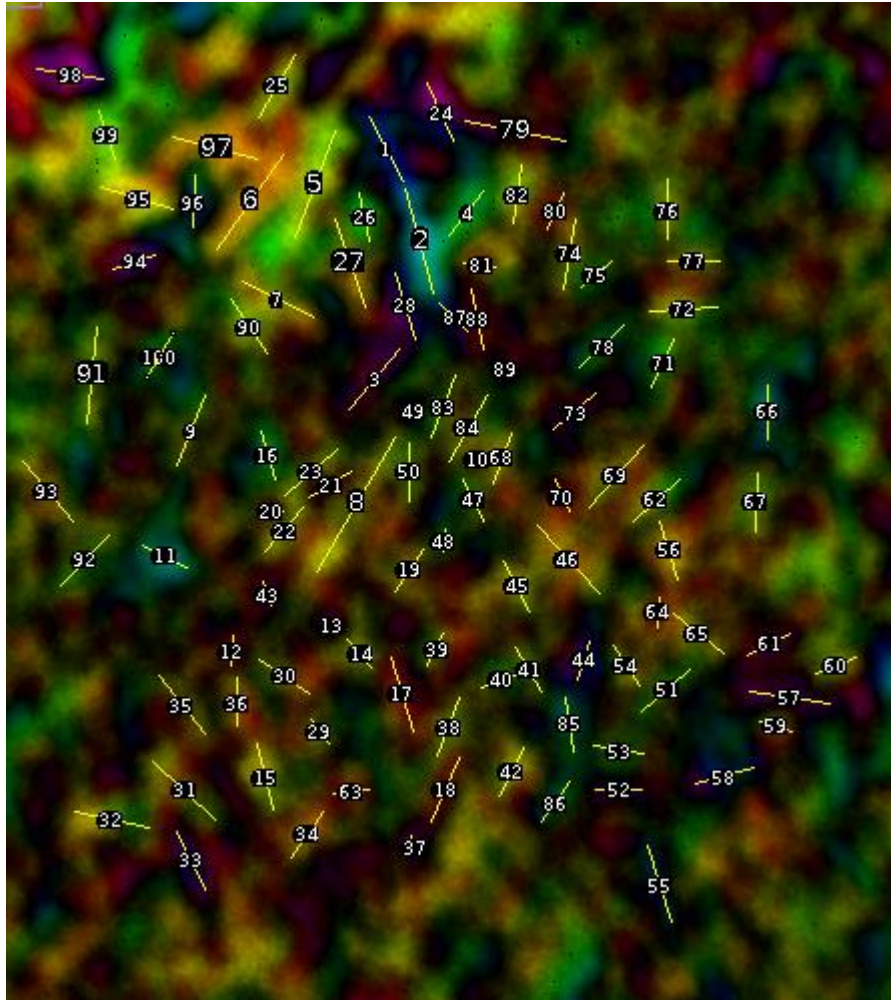


Figure A2: Subset of Figure 9(b) showing particle length measurements. The results of these measurements are shown in Table 2. Particles 1-40 were also used for the analysis of angular distance between neighboring particles, results of which are found in Table 4. Angular distance between particles mapped in PIC mapping was calculated according to Pokroy et. al. (2015).



Figure A3: Reflected light micrograph with crossed polarizers of ooid sample analyzed with PEEM. The diameters of all ooids in the sample were measured, as shown in Table 3.

TABLE 1:

Ooid Laminae Thicknesses			
Label	Length (nm)	Label	Length (nm)
1	2364.035	15	830.028
2	1825.127	16	1931.231
3	2773.454	17	2329.323
4	1375.14	18	1565.58
5	994.557	19	1453.811
6	1003.294	20	922.472
7	1144.186	21	1106.704
8	1491.836	22	1133.408
9	1001.571	23	1200.714
10	887.205	24	1189.761
11	1089.232	25	819.112
12	917.135	26	887.205
13	972.558	Mean	1312.531
14	917.135	SD	526.558
		Min	819.112
		Max	2773.454

TABLE 2:

Particle Size Measurements

Label	Length (nm)						
1	712.356	31	814.866	61	463.36	91	946.739
2	1045.663	32	732.422	62	609.549	92	679.681
3	759.16	33	619.773	63	352.439	93	765.76
4	526.862	34	536.749	64	285.084	94	420.625
5	1112.083	35	722.749	65	618.792	95	721.654
6	1116.725	36	466.064	66	530.784	96	495.526
7	775.944	37	211.622	67	563.441	97	833.652
8	1496.476	38	614.376	68	507.668	98	649.615
9	717.542	39	341.573	69	793.375	99	494.384
10	173.675	40	419.715	70	333.192	100	487.858
11	489.219	41	496.192	71	513.33	Mean	569.451
12	285.964	42	526.823	72	668.675	SD	223.593
13	163.87	43	239.482	73	527.935	Min	161.812
14	358.041	44	380.723	74	690.649	Max	1496.476
15	656.408	45	547.567	75	389.265		
16	485.437	46	883.892	76	582.524		
17	751.395	47	451.639	77	491.952		
18	680.843	48	208.732	78	590.559		
19	493.695	49	161.812	79	996.448		
20	252.614	50	556.785	80	373.447		
21	482.906	51	619.232	81	313.097		
22	570.837	52	440.129	82	582.165		
23	674.041	53	484.227	83	647.831		
24	614.478	54	472.137	84	739.395		
25	704.908	55	775.755	85	537.373		
26	481.103	56	593.919	86	472.536		
27	904.761	57	792.768	87	394.759		
28	665.912	58	584.14	88	602.666		
29	291.262	59	323.625	89	172.381		
30	576.379	60	426.694	90	638.197		

TABLE 3:

Ooid Size

Smallest dimension (pixels)	Largest dimension (pixels)	Size (pixels)	Size (μm)
705	852	778.5	519
760	838	799	532.6667
806	926	866	577.3333
709	925	817	544.6667
779	919	849	566
671	858	764.5	509.6667
657	713	685	456.6667
606	729	667.5	445
802	970	886	590.6667
811	914	862.5	575
846	856	851	567.3333
697	842	769.5	513
857	959	908	605.3333
642	770	706	470.6667
711	777	744	496
790	856	823	548.6667
843	853	848	565.3333
545	728	636.5	424.3333
602	852	727	484.6667
713	959	836	557.3333
667	785	726	484
810	849	829.5	553
820	939	879.5	586.3333
702	768	735	490
732	890	811	540.6667
732	872	802	534.6667
733	957	845	563.3333
652	805	728.5	485.6667
721	896	808.5	539
682	920	801	534
824	924	874	582.6667
735	896	815.5	543.6667
866	894	880	586.6667
			532.5152 Mean
			45.72017 STD

TABLE 4:

particle #	c'	a	b	d	neighbors	boundary	a1	b1	c1	a2	b2	c2	Delta	c
1	23.9	105.5	89.246	0.845934	2,24,5,26	1,2	105.5	89.3	23.9	95.8	114	-1.3	16.08739	
2	-1.3	95.82	114	1.189731	4,28,26	1,24	105.5	89.3	23.9	94.5	82.5	62.5	20.37965	
3	63.4	118.07	51.83	0.438977		1,5	105.5	89.3	23.9	84.8	153.2	-51.5	50.31785	
4	-23.7	83.85	113.52	1.353846		1,26	105.5	89.3	23.9	89.2	129.5	-31.1	34.84143	
5	-51.5	84.8	153.2	1.806604	26,27,6,25	2,4	95.8	114	-1.3	83.85	113.5	-23.7	14.85338	
6	-68.7	85.8	160	1.864802		2,28	95.8	114	-1.3	101.9	56.9	47.1	28.20973	
7	-59.6	94.5	125.18	1.324656		2,26	95.8	114	-1.3	89.2	129.5	-31.1	20.24079	
8	-60.7	101.5	112.55	1.108867	21,22,19a	3,28	118.1	51.83	63.4	101.9	56.9	47.1	7.280559	
9	-46.6	111	70.2	0.632432		5,26	84.8	153.2	-51.5	89.2	129.5	-31.1	16.44294	
10	-69.7	123.9	83.8	0.676352		5,27	84.8	153.2	-51.5	94.6	102.2	-62.6	15.94968	
11	-6.8	98.4	89.2	0.906504		5,6	84.8	153.2	-51.5	85.8	160	-68.7	13.47639	
12	-88.1	115.3	65.14	0.564961	30,36	5,25	84.8	153.2	-51.5	94	125	-60.6	11.25626	
13	66	122.2	46.3	0.378887		6,7	85.8	160	-68.7	94.5	125.2	-59.6	12.3087	
14	-56	102	84	0.823529	17,13	8,21	101.5	112.6	-60.7	127	66.7	-78.4	15.54287	
15	-58.2	104	113	1.086538	36,29,29a,34a,34	8,22	101.5	112.6	-60.7	109	107	-59.7	2.62755	
16	-28.4	103.6	77.8	0.750965	20,23	8,19a	101.5	112.6	-60.7	97.7	98	-74.7	8.553688	
17	-83.9	110	97	0.881818	14,38,39	9,11	111	70.2	-46.6	98.4	89.2	-6.8	20.599	
18	-79.3	116	88	0.758621	38,37	12,30	115.3	65.14	-88.1	114	91.2	-59	14.68207	
19	-63.5	95.3	85.8	0.900315	19a	12,36	115.3	65.14	-88.1	106.8	109.1	-71.4	13.04435	
19a	-74.7	97.7	98	1.003071		13,14	122.2	46.3	66	102	84	-56	45.76205	
20	-74.5	121.5	56.7	0.466667	21,22,23,16	14,17	102	84	-56	110	97	-83.9	14.8094	
21	-78.4	127	66.7	0.525197	22,23	15,36	104	113	-58.2	106.8	109.1	-71.4	7.915299	
22	-59.7	109	107	0.981651	20,21	15,29	104	113	-58.2	115.5	89.3	-57.1	6.520346	
23	-56.4	103	84.2	0.817476	21,20,16	15,29a	104	113	-58.2	106.9	100.9	-74.9	10.09714	
24	62.5	94.5	82.5	0.873016		15,34	104	113	-58.2	99	122.8	-70.8	8.387949	
25	-60.6	94.2	125.4	1.33121		15,34a	104	113	-58.2	131.6	38.3	82.1	52.06129	
26	-31.1	89.151	129.5	1.452592		16,20	103.6	77.8	-28.4	121.5	56.7	-74.5	21.16661	
27	-62.6	94.6	102.2	1.080338		16,23	103.6	77.8	-28.4	103	84.2	-56.4	14.27127	
28	47.1	101.9	56.9	0.558391		17,38	110	97	-83.9	109.8	97	-56.8	14.59529	
29	-57.1	115.5	89.3	0.77316	29a	17,39	110	97	-83.9	116.4	82	-54.3	15.52934	
29a	-74.9	106.9	100.9	0.943873	29,30,15	18,37	116	88	-79.3	63.6	123.6	37.2	70.5662	
30	-59	114	91.2	0.8	29a,12,36	18,38	116	88	-79.3	109.8	97	-56.8	11.99713	
31	-62.8	104.65	101	0.965122	32a,32b,33	19,19a	95.3	85.8	-63.5	97.7	98	-74.7	6.638425	
32	-49.2	110.9	70.5	0.635708	32a	20,21	121.5	56.7	-74.5	127	66.7	-78.4	2.184721	
32a	-62.4	96.9	112.8	1.164087	31,32,32b	20,22	121.5	56.7	-74.5	109	107	-59.7	13.62103	
32b	-77.6	108.35	76	0.701431	33,32a,31	20,23	121.5	56.7	-74.5	103	84.2	-56.4	11.6208	
33	54.6	131.9	55.3	0.419257		21,22	127	66.7	-78.4	109	107	-59.7	13.66288	
34	-70.8	99	122.8	1.240404		21,23	127	66.7	-78.4	103	84.2	-56.4	12.25457	
34a	82.1	131.6	38.3	0.291033	15,31,35	26,27	89.2	129.5	-31.1	94.6	102.2	-62.6	21.4637	
35	-63.8	116.1	79.7	0.686477	36,31	27,28	94.6	102.2	-62.6	101.9	56.9	47.1	50.60985	
36	-71.4	106.8	109.1	1.021536	30,12,15,35	29,29a	115.5	89.3	-57.1	106.9	100.9	-74.9	10.13487	
37	63.6	123.6	37.2	0.300971		29a,30	106.9	100.9	-74.9	114	91.2	-59	9.056943	
38	-56.8	109.8	97	0.883424	17,18	30,36	114	91.2	-59	106.8	109.1	-71.4	8.212973	
39	-54.3	116.4	82	0.704467		31,32a	104.7	101	-62.8	96.9	112.8	-62.4	3.991605	
39a	-81.5	106	96.5	0.910377	40,39,38	31,32b	104.7	101	-62.8	108.4	76	-77.6	9.571132	
40	-43.4	109.81	73.36	0.668063		31,33	104.7	101	-62.8	131.9	55.3	54.6	48.19639	
						32,32a	110.9	70.5	-49.2	96.9	112.8	-62.4	13.18194	
						32a,32b	96.9	112.8	-62.4	108.4	76	-77.6	12.73198	
						34a,35	131.6	38.3	82.1	116.1	79.7	-63.8	44.66734	
						35,36	116.1	79.7	-63.8	106.8	109.1	-71.4	8.176078	
						39a,39	106	96.5	-81.5	116.4	82	-54.3	14.6464	
						39a,38	106	96.5	-81.5	109.8	97	-56.8	13.43661	
						39a,40	106	96.5	-81.5	109.8	73.4	-43.4	19.87519	
						38,40	109.8	97	-56.8	109.8	73.4	-43.4	8.240957	

REFERENCES

Pokroy, B., Kabalah-Amitai, L., Polishchuk, I., DeVol, R.T., Blonsky, A.Z., Sun, C.Y., Marcus, M.A., Scholl, A. and Gilbert, P.U., 2015. Narrowly distributed crystal orientation in biomineral vaterite. *Chemistry of Materials*, 27(19), pp.6516-6523.